Deterministic 3D Ground Motion Simulations (0-5 Hz) and Surface Topography Effects of the 30 October 2016 M_w 6.5 Norcia, Italy Earthquake

[1]Arben Pitarka, [2]Aybige Akinci, [2]Pasquale De Gori, and [2]Mauro Buttinelli

(1) Lawrence Livermore National Laboratory, Livermore, California, United States

(2) National Institute of Geophysics and Volcanology, Rome, Italy

Coresponding Author:

Arben Pitarka

Email:pitarka1@llnl.gov

The authors acknowledge that there are no conflicts of interest recorded

ABSTRACT

The M_w 6.5 Norcia, Italy earthquake occurred on 30 October 2016 and caused extensive damage to buildings in the epicentral area. The earthquake was recorded by a network of strong-motion stations, including 14 stations located within a 5 km distance from the two causative faults. We used a numerical approach for generating seismic waves from two hybrid deterministic and stochastic kinematic fault rupture models propagating through a 3D Earth model derived from seismic tomography and local geology. The broadband simulations were performed in the frequency range of 0-5 Hz using a physics-based deterministic approach modeling the earthquake rupture and elastic wave propagation. We used SW4, a finite difference code that uses a conforming curvilinear mesh, designed to model surface topography with high numerical accuracy.

The simulations reproduce the amplitude and duration of observed near-fault ground motions. Our results also suggest that due to the local fault-slip pattern and upward rupture directivity, the spatial pattern of the horizontal near-fault ground motion generated during the earthquake was complex and characterized by several local minima and maxima. Some of these local ground motion maxima in the near-fault region were not observed because of the sparse station coverage. The simulated PGV is higher than both the recorded PGV and predicted PGV based on empirical models for several areas located above the fault planes. Ground motions calculated with and without surface topography indicate that on average, the local topography amplifies the ground motion velocity by 30%. There is correlation between the PGV and local topography, with the PGV being higher at hilltops. In contrast, spatial variations of simulated PGA do not correlate with the surface topography. Simulated ground motions are important for seismic hazard and engineering assessments for areas that lack seismic station coverage and historical recordings from large damaging earthquakes.

INTRODUCTION

A series of medium to large magnitude earthquakes occurred in central Italy between 2016 and 2017, causing casualties and severe damage to villages in the earthquakes source regions (Chiaraluce et al., 2017). The sequence started with the M_w 6.0 Amatrice earthquake on August 24, 2016, and continued with eight seismic events with $M_w > 5.0$. The 30 October 2016 M 6.5 Norcia earthquake was the largest and the last significant event in the sequence.

This earthquake was generated by a normal fault with a complex secondary fault rupture mechanism (Chiaraluce et al., 2017; Scognamiglio et al., 2018). The faulting mechanism is consistent with the extensional tectonic regime in the central Apennines, associated with the Tyrrhenian back-arc basin opening. The central Apennines are part of a thrust-and-fold belt that is subject to regional scale uplift and to a NE-SW extension (Chiaraluce et al., 2004). Individual high mountain ridges are composed of Mesozoic carbonate rocks overlain by continental quaternary deposits (Di Naccio et al., 2019). This zone is one of the most seismically and tectonically active regions in Italy (Galadini and Galli, 2000, 2003; Akinci et al., 2009; Akinci et al., 2010). In the past few centuries, a series of large earthquake ruptures occurred along the central Apennine Mountains, with magnitudes less than 7.0. For example, large earthquakes occurred in the same area on October 7, 1639, January and February 1703 (Galli et al., 2005; Castelli et al., 2016), and the 1859 Norcia earthquake. The M_w6.3 L`Aquila earthquake struck the region in 2009 and was located 50 kilometers south of the 2016 Norcia earthquake (Chiarabba et al., 2009). The repeated occurrence of strong shaking poses a severe threat to all structures, especially for the unreinforced masonary residential buildings built in the last few hundred years, before the implementation of modern building regulations.

The 2016 Norcia earthquake was recorded by many digital stations belonging to temporary and permanent seismic networks deployed immediately after the Amatrice earthquake. Near-fault strong ground motion station locations and corresponding horizontal and vertical component peak ground acceleration (PGA) and peak ground velocity (PGV) are listed in **Table 1**. The unprecedented density of near-fault seismic stations and the high quality of the recorded data made the 2016 Norcia earthquake one of the best-recorded earthquakes in Italy. The highest PGA was observed at station FCC in the earthquake's epicentral area, with the horizontal component of 0.8 g and the vertical component of 0.5 g. These ground motion levels are the largest ever recorded during an Italian earthquake. The observed PGA was larger than the short-period spectral acceleration considered in the building code spectrum, for an M 6.5 earthquake with a return period of 475 years, (Iervolino et al., 2019).

The observation of building damage concentrated on hilltops above the fault rupture and the relatively large ground motions recorded at several sites above the fault indicate localized ground motion amplification. A combination of source effect and wave focusing due to topographic effects may have contributed to this localized amplification. We perform broadband ground motion modeling and simulations for the Norcia earthquake in an attempt to investigate these important effects, and explore the prospect of using physics-based ground motion simulations in the seismic hazard assessment in the region.

We build upon improving previous ground motion simulation of the 2016 Norcia earthquake (e.g. Ojeda et al, 2021). Ojeda et al. (2021) used a hybrid method that applies a deterministic approach for calculating the low-frequency part of the ground motion time history and a stochastic approach for calculating the high-frequency part of the ground motion. Typically the hybrid methods (e.g. Pitarka et al., 2000; Graves and Pitarka 2016; Pischiutta et al., 2021) are successful at predicting the general characteristics of ground motion. However, the stochastic part of the approach is not well suited for studying relationships between the ground motion variability and high frequency source and wave propagation effects. There is an additional limitation at longer periods when 1D velocity models are used instead of 3D models for computing synthetics seismograms. For example, Ojeda et al. (2021) used a 1D layered model in their hybrid simulation of the Norcia earthquake. While helpful in investigating the region-specific source and attenuation parameters and their influence on the simulated ground motions, simulations using 1D models do not include 3D wave propagation effects caused by geologic structural complexities and surface topography on the observed ground motion amplification pattern. This study is the first attempt to perform deterministic 3D high-frequency modeling of the Norcia earthquake, using a physics-based rupture model and a well-constrained local 3D velocity model that incorporates a detailed tomographic model of the underground structure in the Norcia and Castellucio regions (Chiarabba et al., 2018). We used high-performance computing and a fully deterministic approach to compute strong ground motion in the frequency range 0-5Hz. Based on a 3D curvilinear-grid finite-difference formulation, our anelastic wave propagation modeling code allows for accurate representations of three-dimensional shallow structure and surface topography (Petersson and Sjogreen, 2015, 2018).

In the following sections, we describe the geology and the seismicity of the region, and introduce the local velocity model used in our simulations. After an introduction to the rupture model and simulation methodology, we present ground motion simulation results, followed by analysis of goodness of fit between recorded and simulated ground motion. The simulation is compared with observed records and ground-motion models (GMMs) in order to document the performance of the proposed simulation methodology. Next, we show results from our analysis of ground motion sensitivity to slip distribution and local topography. Finally, we summarize our findings and discuss of how the results might be relevant to seismic hazard assessment from normal-faulting earthquakes in central Italy.

GEOLOGY AND SEISMICITY OF THE REGION

The 2016 Norcia earthquake occurred in the Central Apennines region in Italy. The earthquake was generated by predominantly normal faulting. The Central Apennines region is characterized by the stacking of the Meso-Cenozoic sedimentary successions of the Lazio-Abruzzi calcareous platforms and Umbria-Marche pelagic basins domains, which over-thrusted the calcareous sedimentary successions of the more external Adria plate (Centamore et al., 1993, Bally et al., 1986). During a long history of complex tectonic activity the region has been affected by alternating extensional and compressional regimes which resulted in a complex faulting system. The first set of large-scale normal faults developed mostly during the Mesozoic, as a consequence of the evolution of the Tethys ocean margins realms, while the second set of extensional faults is commonly associated with the Miocene bending of the Adria paleo margin foreland domain before the inset of Apennines compression (e.g Bigi et al., 2013). During the Miocene-Pliocene compressional phase, large-scale thrust developed and contributed to the segmentation and disarticulation of the previous crustal structure (e.g. Barchi et al., 1998). Finally, during the Late Pliocene and Quaternary till present, widespread extension propagated from west to east through the belt, with the development of several intra-chain basins (**Figure 1**) (e.g.,Mazzoli et al., 2000). While the surface topography exhibits a complex fold-and-thrust belt system, a pervasive extension with a predominant northwest-trending affects the whole area, featured by active fault systems bounding the intermountain basins all along the chain (Bosi et al., 2003). Generally, normal faults and thrusts inherited by previous phases, recognized both at the surface or depth, show evidence of being repeatedly reworked during the orogen development, with subsequent episodes of tectonic inversions (e.g. Buttinelli et al., 2018,).

Seismological and geophysical observations show that recent earthquakes are expressions of the reactivation of pre-existing thrust and normal fault structures (e.g., Chiarabba and Amato, 2003, Buttinelli et al., 2018, 2021), rupturing 10 to 25-km-long contiguous fault segments, and reactivating a 150 km-long section of the belt. The central Apennines are characterized by a high seismogenic potential, mainly expressed by shallow (5 to 15 km) earthquakes with predominant normal faulting mechanism, with magnitudes up to 6.5-7. The observed seismicity pattern testifies for a complex interaction between adjacent faults and triggering phenomena (Scognamiglio et al., 2018; Michele et al., 2020) such as static and dynamic stress transfer between faults and pore fluid pressure migration (Chiarabba et al., 2009; Malagnini et al., 2012). Consequently, repeatedly reactivated faults may cause additional fault segmentation, enhancing the overall structural complexity, which in turn have a big impact on the dynamic rupture evolution of large shocks like those recently observed (Cheloni et al., 2017; Scognamiglio et al., 2018).

Paleo-seismic evidence of surface faults, such as the faults that were activated during the Norcia earthquake, highlights the prominent role of normal fault complex networks in the seismic activity. In the past three decades, before 2016-2017, the central Apennines region has been affected by two major normal faulting seismic sequences, the 1997 M_w6.0 Colfiorito and 2009 M_w6.1 L'Aquila, respectively. The M_w6.5 Norcia earthquake represents the largest earthquake of a new sequence that began on August 24, 2016 with the M_w6 Amatrice earthquake.

VELOCITY MODEL

The regional 3D velocity model used in our simulations covers an area 102 km by 88 km and extends to a depth of 31 km (Figure 2). It was constructed by embedding the velocity models of

Norcia basin developed by Di Giulio et al., (2020) and Castelluccio inter-mountain basins, developed by Brozzetti et al. (2019), in the regional tomographic model of the upper crust developed by Chiarabba et al., (2018) for the Amatrice-Norcia region using P and S arrival times for about 44,000 aftershocks that occurred between August 24, 2016 and end of June 2017 in the Amatrice-Norcia region. The central part of the tomographic model, where most of the seismicity is located, has higher P-wave speeds compared to the surounding regions. At shallow depths (0-3 km), lower seimic wave velocities characterize the carbonate rocks of mountain ranges, associated with Pliocene synorogenic formations on top of thrust units. The velocity model of the Castelluccio basin was based on the interpretation of geological cross sections compiled by Pierantoni et al., (2013). The Castelluccio basin is characterized by soft sediments with a maximum thickness of about 200 m-400 m. The V_p and V_s assigned to the sedimentary layers are 2.24 km/s and 0.80 km/s respectively. The Norcia basin has a depth that varies between 100-200 m (**Figure 2**). The V_p and V_s in the alluvial sediments are 1.16 km/s and 0.4 km/s, respectively. The quality factors were computed by the relations $Qs = 0.05V_s$ (for V_s in m/s), in the upper 2km, and $Qs = 0.1V_s$ below 2 km, and $Q_p = 2Q$s (Day and Bradley, 2001; Graves and Day, 2003).

The integration of the tomographic and basins models, into a single velocity model covering the computational domain was done in two steps:

In a first step we interpolated the original tomographic model on a rectangular grid, with variable spacing in the vertical direction. The grid spacing was set to 300 m and 250 m along the north-south direction and along the east-west direction, respectively. The vertical grid spacing was set to 50 m, and 200 m for the depth ranges 0-1 km and 1-16 km, respectively. The vertical grid spacing was chosen to fully represent the depth resolution of both original velocity models.

In a second step we embedded the basin models into the tomographic model using an interpolation scheme similar to that used in the tomographic inversion of Haslinger (1998) where the velocity at a given point is determined by a linear interpolation among the eight surrounding grid points. The final velocity model also includes the surface topography. Cross-sections of the assembled velocity model are illustrated in **Figure 2**. In the near surface layers we set the minimum grid spacing of 25 m and cap the minimum shear wave velocity to 0.6 km/s. With these parameters our finite-difference method produces accurate results of up to 5 Hz.

KINEMATIC RUPTURE MODEL AND GROUND MOTION MODELING METHOD

In this section we describe the kinematic rupture simulation of the Norcia earthquake. The simulation was designed to investigate the performance of our physics based simulation method at reproducing the recorded motion, and address the impact of the earthquake rupture and surface topography on the observed and simulated ground motion amplification patterns.

Kinematic rupture model

The kinematic rupture model used in our simulations was generated using the Graves and Pitarka (GP) technique (Graves and Pitarka, 2016). The GP rupture generator uses spatial and temporal kinematic rupture parameters that are calibrated using observed rupture kinematics. GP has been validated through comparisons of simulated broadband ground motions against ground-motion models, as well as through direct comparisons with a large number of crustal earthquakes in California and Japan (Graves and Pitarka, 2010; Graves and Pitarka, 2016; Pitarka et. al.,2019). The rupture process is randomly heterogeneous at different scale lengths. The resulting multi-scale rupture model incorporates small and large-scale stochastic rupture variability, deterministic large slip areas (e.g., Pitarka et al., 2019), and depth dependent rupture velocity and slip rate (Graves and Pitarka, 2015). These fundamental rupture features, including their depth dependency, were included in the kinematic rupture model used in this study. Detailed explanations of the spatial variation of our kinematic rupture model parameters can be found in Graves and Pitarka (2016). The general form of the slip-rate function $\dot{s}(t)$ follows from Liu et al (2006) and is given by

$$\dot{s}(t) = \begin{cases} A[0.7 - 0.7\cos(\pi t/t_0) + 0.6\sin(0.5\pi t/t_0)] & t < t_0 \\ A[1.0 - 0.8\cos(\pi t/t_0) + 0.2\cos(\pi(t - t_0)/(t_d - t_0))] & t_0 \le t < 2t_0 \, , \\ A[0.2 + 0.2\cos(\pi(t - t_0)/(t_d - t_0))] & 2t_0 \le t < t_d \end{cases} \quad (4)$$

where t_d is the total duration, t_0 is the time at which the peak slip-rate occurs and A is scaled to produce the desired final slip amount. $t_0 = \beta t_d$. β is a fixed parameter that allows the t_0, and consequently the shape of the source time function, to vary with depth. β has the following depth dependency

$$\beta = \begin{cases} 0.5 & z < 1 \text{ km} \\ 0.13 & z > 3 \text{ km} \end{cases} \quad (5)$$

with a linear transition between crustal depths of 1 and 3 km. This formulation allows the shape of the source time function to transition from “cosine-type”, in the depth interval 0-1 km to “Kostrov-type” at depths > 3 km”.

The kinematic rupture model uses a two segment fault model based on the rupture model proposed by Scognamiglio et al. (2018) obtained through a joint inversion of geodetic and seismic data. In our model the main segment has a fault length of 26 km, and a down-dip width of 15 km. This fault length which is shorter than the fault length used in Scognamiglio et al. rupture modeling was chosen to reflect the fact that slip was negligible in the northern portion of the main fault. The second segment has a fault length of 10 km, and a down-dip width of 14 km. The depths to top of the faults are 0.0 and 2.4 km, and the corresponding strikes of each segment are N155^o and N210^o, respectively. The hypocenter is located at 13.12^o longitude, 42.84^o latitude, and 9.5 km depth. The maximum co-seismic slip of about 3 m is concentrated in two prominent patches, one on each fault segment. The location and size of these lage slip patches in our model is based on the slip model of Scognamiglio et al. (2018). We used an average rupture speed of 80% V_s, based on previous studies of the earthquake. The earthquake focal mechanism was assumed to be predominantly normal slip. The rake angle includes small spatially correlated random perturbations of up to 8%, computed following the GP method. **Table 2** provides details of the individual fault segments. **Figure 3** plots the slip distribution, peak slip rate, rise time, and rupture time contours. Note that, constrained by observations and physics-based rupture modeling, the `slip rise time and rupture velocity are depth dependent. The longer rise time at shallow depths and shorter rise time at deeper depths affect the long- and short-period seismic energy content generated by the earthquake rupture.

Ground Motion Modeling Technique

The 3D numerical techniques of wave propagation modeling are capable of producing realistic ground motion. They incorporate source's physics and solve the elastic and anelastic seismic wave equation in a complex media. However, large-scale simulations require high-performance computing (HPC) systems (e.g., Frankel et al., 2018; Toborda and Bielak, 2013; Pitarka et al., 2015; Rodgers et al., 2018). The latest developments in numerical methods and improvements in computing power have led to reliable ground motion simulations of past and future earthquakes. These simulations are contributing to rapid improvements of ground motion data bases for large earthquakes, especially for short distances (<20 km) where the number of worldwide records is relatively small (e.g., McCallen et al. 2020a; McCallen et al. 2020b; Petrone et al., 2021).

In this study, the ground motion velocity is computed using SW4, a time-domain 4^{th} order accurate in space and time finite difference code, based on the summation-by-parts principle (Sjogreen and Petersson, 2012). SW4 is very efficient at modeling anelastic wave propagation in heterogeneous media with anisotropy. It uses a near-surface curvilinear mesh with depth-dependent refinement

(Wang and Petersson, 2019) which allows for accurate implementation of free surface boundary conditions with surface topography (Petersson and Sjogreen, 2015), and accurate wave propagation modeling in heterogeneous media. The simulations were performed by running the parallelized CPU version of the code on Quartz supercomputer at Lawrence Livermore National Laboratory. Simulation with the local 3D velocity model and surface topography were performed on 108,000 CPUs, and required a wall time of 21 hrs. Simulations with flat free surface were performed on 3600 CPUs with a wall time of 4.5 hrs.

The model domain used in the simulations covers an area 102 km by 88 km and extends to a depth of 31 km. This region includes all of the 41 stations shown in **Figure 1** and a rectangular grid of fictitious stations with 1 km spacing covering the entire model area. We use a minimum grid spacing of 25 m and a minimum shear wave velocity of 1000 m/s, which yields reliable results up to a maximum frequency of 5 Hz. Anelastic attenuation is modeled using a constant-Q approximation (e.g., Graves and Day, 2003; Day and Bradley, 2001), and the ground motion acceleration time histories were obtained by differentiating the computed velocity time histories.

GROUND MOTION SIMULATION RESULTS

In this section we describe results of our ground motion modeling and simulations. We used ground motion recorded at 41 stations located in our study area, and ground motion predictions made with GMMs proposed for Central Italy to validate our modeling methodology. In our analysis we used direct waveform comparisons, as well as RotD50 (Boore, 2010) spectral acceleration responses to also investigate the impact of the slip distribution and topographic effects on observed and simulated ground motion in the frequency range 0-5Hz.

Figure 4 and **Figure 5** compare simulated and recorded three-component ground motion velocity and acceleration, respectively, at 36 selected stations, low-passed filtered at 5 Hz. Given that the slip distribution in our rupture model was obtained by combining deterministic features, such as large-slip patches, and random small-scale variations, and no attempt was made to find the rupture model that produces the best waveform fit, we recognize that the simulated motions cannot match all the details of the observed waveforms, especially at high frequencies (> 2Hz). Nonetheless, the simulation does well in matching the velocity time histories at several stations, including near-fault sites (e.g. CLO, FCC, NOR) as well as distant sites (e.g., FOPC, MDAR, NCR, SPD, SPM). Stations FCC (A soil category site), and CLO (B soil category site), are located above the fault rupture plane. The simulated ground motions in terms of averaged horizontal PGV for these sites (FCC and CLO) are 50.9 cm/s, and 42.15 cm/s, while the observed values are 48.5 cm/s, and 52.19 cm/s respectively. Simulations at one of the intermediate distance stations MDAR (B soil category site) at R_{jb} = 27 km resulted in PGV of 4.22 cm/s on the EW component, and 4.49 cm/s on the NS component, while the observed values were 4.1 cm/s 4.29 cm/s, respectively. As for the acceleration, overall, the simulation reproduces the frequency content, peak amplitude, and duration of the observed waveforms. We note that, especially at long distances, the vertical component of simulated acceleration is higher than the recorded acceleration. This single-component overestimation suggests that the velocity model used in our simulations may be deficient in small scale heterogeneities. Small-scale structural heterogeneity, combined with wave conversions and other surface topography effects can enhance near-surface wave scattering effects which in turns reduces the amplitude of surface waves (e.g., Imperatori and Mai, 2015; Rodgers et al., 2010; Hirakawa et al., 2016).

Figure 6 compares recorded and simulated 5% damped RotD50 (Boore, 2010) pseudo spectral accelerations (SA). In order to compare 3D and 1D wave propagation effects on the simulated ground motion, in **Figure 6** we also show response spectra calculated with the 1D model of the

Central Italy (CIA 1D) (Herrmann et al. 2011). As in the 3D simulation, the 1D simulation includes the surface topography. A comparison of the CIA 1D model and the 1D velocity column obtained from the 3D velocity model at the epicenter is shown in **Figure 7**. The simulated response spectra indicate that the largest difference between the two sets of synthetics is mainly observed et periods smaller than 1s. Depending on the stations location, the amplitude of synthetics obtained with the 1D model is 5%-15% higher than that of synthetics obtained with the 3D model. This relatively small difference could be explained by the similar wave propagation effects produced by the two models due to their similar velocities in the depth range 4-20 km, and the oevarll weak lateral velocity variations in the shallow part (< 4km) of the 3D model.

To quantitatively evaluate the overall performance of our numerical simulations and the predictive capability of our method we calculated residuals between the recorded and simulated RotD50 spectral acceleration using the 3D model. We used the goodness-of-fit (GoF) (e.g. Graves and Pitarka, 2010) between the recorded and simulated 5% damped pseudo-spectral acceleration RotD50 value (Boore, 2010), with the residual for each site j as a function of period T_i given in the natural log domain as

$$r_j(T_i) = \ln\left[O_j(T_i)/M_j(T_i)\right], \tag{1}$$

where and O_j and M_j are the observed and modeled responses, respectively. The model bias is then given by

$$B(T_i) = \frac{1}{N}\sum_{j=1,N} r_j(T_i) \tag{2}$$

and the standard deviation by

$$\sigma(T_i) = \left\{\frac{1}{N}\sum_{j=1,N}\left[r_j(T_i) - B(T_i)\right]^2\right\}^{1/2},$$

where N=41 is the number of stations.

Figure 8 plots the model bias and standard deviation over the period range 0.2 - 10 s, averaged over all 41 stations. We limit the shortest period to 0.2 s in order to be compatible with the period range 0 – 5 Hz of our simulations. The near zero bias over a broad period range suggests that, on average, our simulated ground motion matches the recorded one. The standard deviation of the bias, indicated by the dotted line, is relatively higher at periods shorter than 3s and remains lower at long periods (> 3s). This feature indicates that there is a non-negligible uncertainty in our ground motion simulations in the short period response due to the unknown small-scale heterogeneities in the earthquake rupture model and shallow crust velocity model.

Comparison with Ground-Motion Models

To examine how the ground motion characteristics compare to ground-motion models (GMMs) for Central Italy (Bindi et al., 2011), in **Figure 9** we show the comparison of PGA, PGV and SA at 2.0 s (SA2.0) between the recorded and simulated data, low-pass filtered at 5Hz, and the GMMs. The GMMs are calculated for M6.5, normal-faulting using estimates for different site conditions, classified as A, B, and C, according to Eurocode 8, EC8 (CEN 2004), representing rock, hard soil, and soft soil types, respectively. The comparison indicates that the GMMs predict well the PGA, PGV and SA2.0 at very short fault distances. However for the type B and C sites the GMMs overpredict both recorded and simulated ground motion at fault distances larger than 5km. The overprediction is more pronounced for the PGA and SA0.2 than for the PGV. Also the simulated PGA is slightly lower than the recorded PGA. This is probably due to the limited high frequency content in our synthetics imposed by the numerical accuracy of our simulations. It is important to note the observed ground motion as well as the simulated ground motion is similar to the GMMs predictions trend with distance. However significant differences are observed at very short distances where the ground motion amplitude displays sharp spatial variations over the fault plane's hanging-wall section. As it will be discussed below, high PGA values observed at sites located above the fault could be an expression of combined effects of large slip patches and local wave focusing due to surface topography.

Topographic Effects

Recent studies of the Norcia earthquake damage (Galli et al., 2017; Costanzo 2018; Rossi et al., 2018) have indicated that in the heavily damaged zone there was evidence of increased damage to old masonry buildings in villages located on hilltops (Liberatore et al., 2019). Studies of recorded (e.g., Celebi, 1987; Pitarka and Irikura, 1996; Spudich et al., 1996; Geli et al., 1988; Hough et al., 2010; Shafique et al., 2011) and simulated (Bouchon et al., 1996; Rodgers et al., 2010; Imperatori and Mai, 2015; Lee et al., 2008) topographic effects have suggested that the ground motion amplification and de-amplification patterns caused by the surface topography are expressions of interferences of free-surface and near free-surface converted and reflected waves. Being dependent on the frequency content of the incoming waves, size of topography, and near-surface material properties, the surface expression of these interferences can have a complex pattern (e.g. Bouchon et al., 1996; Geli et al., 1998; Imperatori and Mai, 2015). In this study we investigated the possible implication of topographic effects in the spatial ground motion amplitude pattern observed during the earthquake.

One common way of extracting the surface topography effects using strong ground motion modeling is by examining relative differences between ground motions computed with and without surface topography. This was applied to the whole modeled frequency range between 0 and 5 Hz. The comparison of simulated time histories of ground motion velocity at four selected stations FCC, PRE, CLF, and CIT, located in the epicentral area, is illustrated in **Figure 10**. The ground motion comparison at these selected sites sugests that the presence of surface topography enhances the near-surface wave scattering which creates local PGV maxima and minima, caused by constructive and deconstructive interferences of different types of waves. These effects are also discernible in **Figure 11** where we plot snapshots of the vertical component of wavefields extracted from the simulations with (TOPO) and without (FLAT) topography, at 13.0s and 15.7s into the earthquake. The isochromatic fringe patterns are different between the wavefronts simulated without and with topography, with the TOPO case being more irregular. The distinct difference in small-scale features between the two models suggests that the wave scattering effect caused by the surface topography breaks the coherency of different wave fronts by creating small-scale spatial amplitude variations.

We used results from our simulations with and without topography to investigate the frequency range of ground motion amplification caused by the surface topography. Similar to the goodness of fit plot shown in **Figure 8**, in **Figure 12** we show the 5% SA RotD50 goodness of fit using acceleration response spectra computed with a flat free surface. It is clear that in this case the synthetics underestimate the ground motion. The positive shift of the bias caused by the spectral acceleration misfit indicates that the neglected topographic effects account for about 35% of the recorded ground motion amplitude at frequencies higher than 1Hz. The rather broad frequency range of the surface topography effect obtained here may concern a variety of structures with response periods shorter than 1s.

The bias observed at periods longer than 5s could be caused by a probable inaccurate representation of the wave propagation attenuation in our 3D velocity model, or inadequate long period seismic energy generated by the proposed rupture model. The fact that the discrepancy is stronger in the presence of the topography (see **Figure 8**) suggests that it may be linked to the wave propagation model, including the attenuation, rather than the source model. Note that the

3D model with flat topography was obtained from the original 3D velocity model by simply flattening the free surface. The free surface flattening changes the depth of layers interfaces relative to the free surface which consequently may alter 3D wave propagation effects, even at longer periods.

We investigated the spatial variation of the PGA and PGV and their possible correlations with topography features such as local peaks and troughs. Using our Norcia earthquake simulations with and without surface topography we computed synthetic ground motion on a dense grid of stations with 1km spacing covering the entire computational domain. Then at grid points along two orthogonal lines A-A'- and B-B', crossing the epicenter, we computed the ratio between ground motions obtained with and without topography, for PGV and PGA, respectively. The ratios are shown in **Figure 13**, together with the corresponding ground surface elevation, high-pass filtered at the elevation variation length of 10 km. The filtering was used to remove large-scale ground elevation variations with lengths longer than 10km. The comparison shows that the PGV correlates with local variations of surface topography, regardless of the site location. The local maxima of the PGV ratio correspond with local topography peaks, and PGV ratio local minima correspond to local topography troughs.

To better demonstrate and quantify the spatial distribution of topographic effects on PGV in **Figure 14** we show maps of the simulated horizontal PGV, computed with the reginal 3D model with and without the surface topography. Also shown is a map of the ratio of their respective PGV overlying the surface topography. The map of the PGV ratio shows deamplifications (PGV ratio < 1) in most of the valleys and amplifications with various strength of up to 2.5 on mountains top. As suggested by other studies, one of the main reasons of peak velocity amplifications could be the topography resonance for intermediate-periods waves carrying the PGV (~1s) in hills with a width similar or longer than the corresponding wavelength of 1km (Marzorati et al., 2011; Massa et al., 2010; Spudich et al., 1996; Geli et al., 1998) .

The simulated PGA does not correlate as well as the PGV with topography variations. It is difficult to explain this result without a more detailed analysis of wave propagation scattering using careful designed numerical experiments for the Norcia region. One possible explanation is that each topographic feature (small hill or small valley) acts as a high frequency scatterer. A rough topography can create short-wavelength spatial interferences of free surface-generated waves, with local maxima and minima that do not necessarily reflect individual geometrical characteristics of the topographic element, where the receiver is located. Instead, the high frequency part of the seismograms that carries the PGA may represent the integrated effect of the surrounding topography. Our conjecture is slightly different from the conclusion reached by Maufroy et al., (2015) in their study of ground motion variability due to surface topography. Based on analysis of synthetic waveforms, they found that the amplification caused by focusing and defocusing effects of body waves is correlated with the local curvature of the earth surface. Therefore, the frequency-scaled curvature of the Earth's surface and local V_s can be used to predict the topographic site-effect amplification.

PGV Maps

Being generated on two relatively low dip angle faults with a predominantly normal slip mechanism, the near-fault ground motion variability for the Norcia earthquake is expected to be sensitive to the slip distribution pattern. To better assess the free-surface ground motion pattern and implication of the slip distribution on the PGV amplification pattern we used our simulations with surface topography to compute ground motion velocity at 8712 virtual receivers located on a regular grid covering the entire study area, with a 1 km spacing. Deterministic broad band simulations like the ones performed here have the ability to provide a full picture of the ground motion spatial variability on a broad frequency range (0-5 Hz), which cannot be achieved by hybrid methods that rely on a simplistic stochastic representation of high frequency ground motion. The effects of the slip distribution were investigated using two sets of synthetic ground motion obtained with two rupture models. The first data set was obtained with the M_w6.5 Norcia earthquake rupture proposed in this study (Model 1), and the second data set was obtained with Model 2 a rupture scenario similar to Model 1, but with slightly different locations of the main slip patches. Model 2 is shown in **Figure 15**. The purpose of the second simulation was to demonstrate the sensitivity of the PGV spatial distribution to location of large slip areas for a Norcia type scenario earthquake rupture.

Figure 16 compares maps of the horizontal PGV computed with the two rupture models. The map covers an area centered on the fault region. It is clear that the ground motion amplification pattern depends on the relative location of the large slip patches. The Norcia earthquake PGV map is dominated by four areas with relatively large PGV, located above the faults surface projection. In these areas PGV reaches values of up to 200 m/s. Three of the large PGV areas, located to the east, south and south east of the epicenter, in which the damage during the earthquake was also high, are most likely created by the upward and lateral rupture directivity effects, as expected for a normal faulting rupture initiated near the bottom of both fault segments. We do not have a clear explanation for the fourth high PGV area located west of the epicenter, other than focusing due to the earthquake radiation pattern.

The location of the high PGV areas and their amplitude change depending on the location of the large slip areas in the model. Due to a drop in peak ground velocity the large PGV areas become more connected to each other and the large PGV area to the south of the epicenter increases in size. Produced by potential rupture directivity effects for this type of rupture (e.g. Tinti et al., 2016) , these PGV features are a direct consequence of the location of the large asperity areas. These results clearly show that, although affected by the local topography, the lateral extent of the PGV mainly reflects the upward rupture directivity effect, which in the case of a shallow dipping fault makes the ground motion amplification more correlated with the fault's large slip pattern. A similar conclusion was reached by Paolucci et al. (2015) based on long period ground motion simulations of the M_w6.0 2012 May 29 Po Plain, Italy earthquake. Our PGV maps demonstrate that for future earthquakes in the central Apennines the near-fault ground motion velocity is expected to be higher above the fault, especially at hill tops located near large slip patches.

Figure 17 demonstrates the large near-fault fluctuations of the observed and simulated peak ground velocities computed with the TOPO and FLAT models, for both horizontal and vertical ground motion components. In this figure we show the median ground motion and its standard deviation obtained for all receivers on the regular grid, and for fault distances up to 48 km. It is important to note that there is a sharp increase in ground motion variability in the fault distance range 2-10 km. A similar trend is seen in the recorded PGV, although the wavefield spatial sampling with strong motion stations is very sparse. The simulated near-fault ground motion variability suggests that due to its insufficient spatial density, the network of stations that recorded the main shock may have missed the largest ground motion generated during the Norcia earthquake. These PGV plots suggest that for a normal slip earthquake on a dipping fault the ground motion variability is expected to be high in regions above the fault. **Figure 17** also shows that, as discussed before, at fault distances larger than 6 km, the simulated vertical PGV is higher than the recorded PGV. Since this discrepancy is only observed on the vertical component of motion and becomes more pronounced away from the fault, we speculate that it has to do with the misrepresentation of shallow wave scattering in our velocity model. Another explanation has to do with the rather uniform normal slip focal mechanism adopted in our rupture model which could affect the vertical component of the simulated ground motion.

The rupture model used in our simulations of the Norcia earthquake is randomly heterogeneous at different scale lengths (see **Figure 3**). It incorporates deterministic features of large slip areas, constrained by inverted fault slip, and large and small-scale stochastic perturbations. In order to assess the sensitivity of the simulated ground motion to small-scale random rupture variations, we performed an additional simulation with a new rupture model, named Model 3. Compared with the original rupture model Model 1, Model 3 contains similar large slip patches but different small-scale variations of the slip, rupture time, rise time, and rake angle, generated with a different random seed. Model 3 and the simulation results, including waveform comparisons, the PGV map and SA RotD50 goodness of fit plot computed as the ratio between Model 1 and Model 3, averaged over all the stations considered in this study, are shown in **Figure 18**.   The very small bias between the two models and its small standard deviation at all periods suggests that the the choice of small-scale random perturbations in our rupture generator does not significantly affect the overall characteristics of the simulated ground motion.

DISCUSSION AND CONCLUSIONS

The objective of this study is twofold: (1) investigate the performance of physics-based fully deterministic ground motion simulations at reproducing the observed ground motion of the M_w6.5 Norcia earthquake. (2) demonstrate that the combined effects of rough topography and fault slip complexity during the earthquake contributed to near-source ground motion variability and amplification, especially at sites above the fault plane. This study is the first attempt to simulate the near-fault ground motion from the 2016 Norcia earthquake, based on a kinematic fault model and a newly developed local 3D velocity model. The simulated ground motion time histories were compared with the recorded ones in the frequency range 0-5 Hz at 41 strong motion stations, located within 30 km of the fault. The simulations were carried out on high-performance computers at Lawrence Livermore National Laboratory in Livermore, California, using a 3D anelastic finite difference method, and a seismic velocity model based on the local geology and the tomographic model of Chiarabba et al.(2018). The near-surface curvilinear grid with a minimum spacing of 25 m used in sampling the surface topography and near-surface underground structure allowed for accurate wave propagation modeling for frequencies up to 5 Hz.

The simulation proved to be reliable in reproducing the recorded ground motion time histories and spectral amplitudes in the modeled frequency range, with a tendency to overestimate the amplitude of the ground motion vertical component. The overestimation can be partially attributed to features of the 3D velocity model, such as lack of granularity and heterogeneity, assumed linear and isotropic soil properties, and partially to the frequency-independent radiation pattern adopted in our kinematic rupture model. Nevertheless, our study confirms that the local wave propagation effects can be reproduced by the 3D wave propagation model used here.

Our simulations suggest that earthquakes on shallow dipping normal faults, like the Norcia earthquake, can produce relatively large ground motion, especially in areas located above the fault, and in proximity to large slip patches. The combination of these rupture propagation effects with the amplification due to local topography can result in large ground motion amplifications with complex spatial variability. This observation is well supported by the characteristics of ground motion recorded by the near-fault stations.

In addition to testing our modeling capability, we carried out numerical experiments aimed at investigating potential topographic effects on the observed amplification pattern. The topographic effects were analyzed by comparing ground motions computed with the local velocity model, with and without surface topography. The contribution of surface topography effects to ground motion amplification was then isolated by computing the ratios of PGV and PGA derived from the models with and without topography, respectively. We found that the spatial variation of the PGV correlates better than that of the PGA with the local variations of topography, with the PGV being higher at mountain peaks and ridges. A plausible explanation of this finding is that, due to short-wavelength spatial interferences of free surface-generated waves, affected by the topography, the high frequency part of the seismogram carrying the PGA at a given location may be shaped by the integrated wave propagation effects of the surrounding topography. Therefore the resulting PGA amplification does not allways reflect the geometrical characteristics of the topographic element, where the receiver is located. Our simulations also suggest that local topography effects can result in ground motion amplifications of up to 30% for periods shorter than 1.5 s. The wide spread topographic effect, mainly manifested as ground motion amplification at hill tops, is likely a significant contributor to the seismic hazard in the region. This conclusion is in agreement with the concentration of severe damage observed during several past earthquakes in Central Italy. Damage inspections for the May 6th 1976, M_w6.4 Friuli, September 26th 1997, M_w6.0, Umbria Marche, and April 6th 2009, M_w6.3, Aquila earthquakes reported that the largest level of shaking and heaviest damage to masonry buildings were mostly observed on hilltops. (e.g. Bramati et al., 1980; Marzorati et al., 2011; Pischiutta et al., 2010; Massa et al., 2010; Magnoni et al., 2014). Although topographic effects using observed ground motion have been the subject of several studies, their investigation has mostly been focused on explaining the damage pattern observed during damaging earthquakes. The recent development of high efficiency numerical methods, like the one used in this study, has opened the way to quantitative estimating of topographic effects, and to building predictive capabilities needed in the seismic hazard assessment in regions with rough topography (e.g.Maufroy et al.,2015). Being controlled by the rupture process (relative locations of the fault and large slip areas, frequency content and direction of the incoming motion) and geotechnical and geometrical characteristics of the topography (material heterogeneity, topography size and roughness) the topographic effects are region dependent. Therefore the transportability of quantitative estimates of topographic effects from one region to another may not always be reliable.

In an effort to demonstrate the sensitivity of near-fault ground motion variability and amplification pattern to fault slip pattern we performed a simulation with a scenario rupture model on the same faults that ruptured during the Norcia earthquake in which the large slip areas in both fault segments were purposely shifted by several kilometers (see **Figure 15**). We observed that the location of large PGV areas is linked to the location of large slip areas. This result suggests that the ground motion amplification pattern of the Norcia earthquake was controlled by both rupture process and surface topography. The highest ground motion is obtained at hilltops in areas above the fault trace. The largest horizontal PGA and PGV observed during the Norcia earthquake were 696 cm/s^2 and 58 cm/s, respectively. At the same location the corresponding simulated values are 512 cm/s^2 and 48 cm/s, respectively. The slightly lower simulated peak values are due to the limited frequency range used in the simulations. Meanwhile, the largest simulated PGV is 150m/s. It corresponds to a mountain top location. This is much higher than the highest value of the observed PGV. Similarly, at several sites the synthetic PGV is higher than the highest observed

PGV. This result suggests that the sparse network of stations that recorded the Norcia earthquake most likely missed the maximum ground motion generated by the earthquake.

The separation of topographic effects from source and wave propagation effects and their individual quantification requires a step-by-step procedure that includes simulations of source, near-surface underground structure and surface topography effects, using models with gradually increasing complexities. Although very important, these quantitative analysis are beyond the scope of this study. Our study is mainly focused on providing simulation-based evidence for ground motion amplification at mountain tops and deamplification in valleys, due to local topography. Our investigation can be helpful in explaining the near-fault building damage pattern observed during the Norcia earthquake.

In conclusion, we found the topography effect to be an important factor that influenced the ground-motion amplification pattern during the Norcia earthquake. We also found that the recorded ground motion variability at near-fault stations was strongly affected by the large slip areas along the fault rupture. This suggests that both the 3D surface topography and large slip areas location are key modeling parameters in seismic hazard assessments for scenario earthquakes in the region. Ground motions calculated using a fully deterministic approach can be used to improve our understanding of the seismic hazard and refine the corresponding seismic risk estimates for scenario earthquakes in the central Apennines.

ACKNOWLEDGMENTS

The study was partially funded by the Italian Presidenza del Consiglio dei Ministri–Dipartimento della Protezione Civile (DPC) Agreement B1, DPC-INGV. This paper does not necessarily represent DPC official opinions and policies. Arben Pitarka's work was performed under the auspices of the U.S. Department of Energy by Lawrence Livermore National Laboratory (LLNL) under Contract DE-AC52-07NA27344. Release: LLNL-JRNL-822363. The simulations were performed on the LLNL's HPC Systems, and were funded by the LLNL Computing Grand Challenge 14 "Broadband Earthquake Ground Motion Simulations on LLNL's Next Generation HPC Systems". We thank Martin Mai and one anonymous reviewer for their carefull reviewes and suggestions that improved the clarity and quality of this article.

DATA AND RESOURCES

The unprocessed acceleration time histories are obtained from the Rete Accelerometrica Nazionale (RAN), managed by the Department of Civil Protection (DPC; http://ran.protezionecivile.it/, last accessed April 2018) and from the INGV International Federation of Digital Seismograph Networks (FDSN) web service (http://webservices.rm.ingv.it/, last accessed April 2018). The processed strong-motion data and station metadata are obtained from the Engineering Strong-Motion (ESM) database (http://esm.mi.ingv.it, last accessed April 2018). A number of figures were created using the Generic Mapping Tools version 4.5.3 (Wessel et al., 2013). Seismic signal analysis was performed using SAC (Seismic Analysis Code) version 101.6 (Goldstein et al., 2003; Goldstein & Snoke, 2005). SW4 computer code was performed to solve the seismic wave equations in displacement formulation using a node based finite difference approach, developed at the Lawrence Livermore National Laboratory (https://geodynamics.org/cig/software).

REFERENCES

Akinci, A., F. Galadini, D. Pantosti, M. Petersen, L. Malagnini, and D. Perkins (2009). Effect of time dependence on probabilistic seismic seismic hazard maps and deaggregation for the central Apennines, Italy, Bull. Seismol. Soc. Am. 99, no. 2A, 585–610.

Bally, A. W., Burbi, L., Cooper, C., Ghelardoni, R., (1986). Balanced sections and seismic reflection profiles across the Central Apennines. Mem. Soc. Geol. It, 35(1), 257-310.

Barchi, M., Minelli, G., Pialli, G.P., (1998). The CROP 03 profile: a synthesis of results on deep structures of the Northern Apennines. Mem. Soc. Geol. Ital. 52, 383–400.

Bigi, S., Casero, P., Chiarabba, C., Di Bucci, D., (2013). Contrasting surface active faults and deep seismogenic sources unveiled by the 2009 L'Aquila earthquake sequence (Italy). Terra Nova, 25(1), 21-29.

Bindi, D., Pacor, F., Luzi, L., Puglia, R., Massa, M., Ameri, G. & Paolucci, R., (2011). Ground motion prediction equations derived from the Italian strong motion database, Bull. Earthquake Eng, 9 (6), 1899–1920, doi:10.1007/s10518-011-9313-z.

Blumetti, A.M., Dramis, F., Michetti, A.M., (1993). Fault-generated mountain fronts in the central Apennines (Central Italy): Geomorphological features and seismotectonic implications. Earth Surf. Process. Landform. 18 (3), 203–223. https://doi.org/10.1002/esp.3290180304

Boore, D. M. (2010). Orientation independent, nongeometric-mean measures of seismic intensity from two horizontal components of motion. Bulletin of the Seismological Society of America, 100, 1830–1835.

Bosi, C., Galadini, F., Giaccio, B., Messina, P., Sposato, A. (2003). Plio-Quaternary continental deposits in the Latium-Abruzzi Apennines: the correlation of geological events across different intermontane basins. Il Quaternario, 16(1Bis), 55-76.

Bouchon, M., Schultz, C.A. & Toksoz, M.N., 1996. Effect of three dimensional topography on seismic motion, J. Geophys. Res., 101(B3), 5835–5846.

Brozzetti, F., Boncio, P., Cirillo, D., Ferrarini, F., De Nardis, R., Testa, A., Lavecchia, G. (2019). High-resolution field mapping and analysis of the August–October 2016 coseismic surface faulting (central

Italy earthquakes): Slip distribution, parameterization, and comparison with global earthquakes. Tectonics, 38(2), 417-439.

Brozzetti, F., Lavecchia, G., (1994). Seismicity and related extensional stress field: The case of the Norcia seismic zone. Ann. Tecton. 8, 38–57.

Buttinelli, M., Pezzo, G., Valoroso, L., De Gori, P., Chiarabba, C. (2018). Tectonics inversions, fault segmentation, and triggering mechanisms in the central Apennines normal fault system: Insights from high-resolution velocity models. Tectonics, 37. https://doi.org/10.1029/2018TC005053.

Buttinelli M., Petracchini L., Maesano F.E., D'Ambrogi C., Scrocca D., Marino M., Capotorti F., Bigi S., Cavinato G.P., Mariucci M.T., Montone P. & Di Bucci D. (2021). The impact of structural complexity, fault segmentation, and reactivation on seismotectonics: constraints from the upper crust of the 2016-2017 Central Italy seismic sequence area. Tectonophysics. (in press).

Calamita, F., Pizzi, A. (1994). Recent and active extensional tectonics in the southern Umbro-Marchean Apennines (central Italy). Memoria y Sociedad Geological Italy, 48, 541– 548.

Castelli, V., Camassi, R., Cattaneo, M., Cece, F., Menichetti, M., Sannipoli, E.A. and Monachesi, G. (2016). Materiali per una storia sismica del territorio di Gubbio: terremoti noti e ignoti, riscoperti e rivalutati. Quaderni di Geofisica, 133, 200 pp.

CEN (European Committee for Standardization) Eurocode 8: design of structures for earthquake resistance, Part 1: General rules, seismic actions and rules for buildings (EN1998-1) 2004 Brussels, Belgium

Centamore, E., Cantalamessa, G., Micarelli, A., Potetti, M., Ridolfi, M., Cristallini, C., Morelli, C., (1993). Contributo alla conoscenza dei depositi terrigeni neogenici di avanfossa del teramano (Abruzzo settentrionale). Bollettino della Società Geologica Italiana, 112(1), 63-81.

Celebi, M. (1987) Topographical and geological amplifications determined from strong motion and aftershock records of the 3 March 1985 Chile earthquake. Bull. Seism.Soc. Am. 77, 1147-1157.

Cheloni, D., De Novellis, V., Albano, M., Antonioli, A., Anzidei, M., Atzori, S., Castaldo, R., (2017). Geodetic model of the 2016 Central Italy earthquake sequence inferred from InSAR and GPS data. Geophysical Research Letters, 44(13), 6778-6787.

Chiarabba, C., De Gori, P., Cattaneo, M., Spallarossa, D., & Segou, M. (2018). Faults geometry and the role of fluids in the 2016–2017 Central Italy seismic sequence. Geophysical Research Letters, 45. https://doi.org/10.1029/2018GL077485l. 2018.

Chiarabba, C., De Gori, P., & Mele, F. (2015). Recent seismicity of Italy: Active tectonics of the central Mediterranean region and seismicity rate changes after the Mw 6.3 L'Aquila earthquake. Tectonophysics, 638, 82– 93. https://doi.org/10.1016/j.tecto.2014.10.016

Chiarabba, C., Amato, A., Anselmi, M., Baccheschi, P., Bianchi, I., Cattaneo, M., et al. (2009). The 2009 L'Aquila (Central Italy) Mw6.3 earthquake: Main shock and aftershocks. Geophysical Research Letters, 36, L18308. https://doi.org/10.1029/2009GL039627.

Chiarabba C. and Amato A. (2003).Vp and Vp/Vs images of the Colfiorito fault region (Central Italy): a contribution to understand seismotectonic and seismogenic processes J. Geophys. Res., 108, 10.1029/2001JB001665.

Chiaraluce, L., Di Stefano, R., Tinti, E., Scognamiglio, L., Michele, M., Casarotti, E., et al. (2017). The 2016 Central Italy seismic sequence: A first look at the mainshocks, aftershocks and source models. Seismological Research Letters, 88(3), 757– 771. https://doi.org/10.1785/0220160221.

Chiaraluce, L., Amato, A., Cocco, M., Chiarabba, C., Selvaggi, G., Di Bona, M., et al. (2004). Complex normal faulting in the Apennines thrust-and-fold belt: The 1997 seismic sequence in central Italy. Bulletin of the Seismological Society of America, 94(1), 99– 116. https://doi.org/10.1785/0120020052.

Civico, R., Pucci, S., Villani, F., Pizzimenti, L., De Martini, P. M., Nappi, R., the Open EMERGEO Working Group (2018). Surface ruptures following the 30 October 2016 Mw 6.5 Norcia earthquake, central Italy. Journal of Maps, 14(2), 151– 160.

Coltorti, M., Farabollini, P. (1995). Quaternary evolution of the Castelluccio di Norcia Basin. Il Quaternario, 8, 149– 166.

Costanzo A. (2018). Shaking maps based on cumulative absolute velocity and arias intensity: the cases of the two strongest earthquakes of the 2016–2017 Central Italy seismic sequence. ISPRS Int J Geo-Information, 7(7): 244. https://doi.org/10.3390/ijgi7070244.

Day, S. M., and C. R. Bradley (2001). Memory efficient simulation of anelastic wave propagation, Bull. Seism. Soc. Am. 91, 520–531.

Di Domenica, A., Turtù, A., Satolli, S., Calamita, F., (2012). Relationships between thrusts and normal faults in curved belts: new insight in the inversion tectonics of the Central-Northern Apennines (Italy). J. Struct. Geol. 42, 104–117. http://dx.doi.org/10.1016/j.jsg.2012.06.008.

Di Giulio, G., Ercoli, M., Vassallo, M., & Porreca, M. (2020). Investigation of the Norcia basin (Central Italy) through ambient vibration measurements and geological surveys. Engineering Geology, 267, 105501.

Di Naccio, D., Kastelic, V., Carafa, M.M., Esposito, C., Milillo, P. & Di Lorenzo, C., (2019). Gravity versus tectonics: the case of 2016 Amatrice and Norcia (Central Italy) earthquakes surface coseismic fractures, J. geophys. Res., 124(4), 994–1017.

Frankel, A., E., Wirth, N. Marafi, J. Vidale, W. Stephenson, (2018). Broadband Synthetic Seismograms for Magnitude 9 Earthquakes on the Cascadia Megathrust Based on 3D Simulations and Stochastic Synthetics, Part 1: Methodology and Overall Results. Bulletin of the Seismological Society of America (2018) 108 (5A): 2347–2369.https://doi.org/10.1785/0120180034.

Galadini, F., and P. Galli (2000). Active tectonics in the central Apennines (Italy)-input data for seismic hazard assessment, Nat. Haz. 22, 225–270.

Galadini, F., & Galli, P. (2003). Paleoseismology of silent faults in the Central Apennines (Italy): The Mt. Vettore and Laga Mts. Faults. Annals of. Geophysics, 46(5), 815– 836.

Galli, P., Galadini, F., Calzoni, F., 2005. Surface faulting in Norcia (central Italy): A "paleoseismological perspective" Tectonophysics 403 (1-4), 117–130.

Galli P, Castenetto S, Peronace E (2017) The macroseismic intensity distribution of the 30 October 2016 earthquake in central Italy (Mw 6.6): seismotectonic implications. Tectonics 36:2179–2191. https://doi.org/10.1002/2017TC004583.

Geli, L., Bard, P. Y. and Jullien, B. (1988) The effect of topography on earthquake ground motion. A review and new results. Bull. Seism. Soc. Am 78, 42-63.

Goldstein, P., Dodge, D., Firpo, M., Minner, L., Lee, W. H. K., Kanamori, H., ... & Kisslinger, C. (2003). SAC2000: Signal processing and analysis tools for seismologists and engineers. The IASPEI international handbook of earthquake and engineering seismology, 81, 1613-1620.

Goldstein, P. A. U. L., & Snoke, A. (2005). SAC availability for the IRIS community. Incorporated Research Institutions for Seismology Newsletter, 7 (UCRL-JRNL-211140).

Graves, R. W. and Day, S. M., (2003). Stability and accuracy analysis of coarse-grain viscoelastic simulations, Bull. Seismol. Soc. Am., 93 (1), 283–300.

Graves, R., and A. Pitarka (2010). Broadband Ground-Motion Simulation Using a Hybrid Approach. Bulletin of the Seismological Society of America, 100(5A), 2095–2123. https://doi.org/10.1785/0120100057.

Graves, R. and Pitarka (2015). Refinements to the Graves and Pitarka (2010). Broadband Ground Motion Simulation Method. Seismol. Res. Lett. 86, no. 1, 1–6, doi: 10.1785/0220140101.

Graves, R., & Pitarka, A. (2016). Kinematic ground motion simulations on rough faults including effects of 3D Stochastic velocity perturbations. Bulletin of the Seismological Society of America, 106, 2136–2153.

Haslinger, F. (1998). Velocity structure, seismicity and seismotectonics of northwestern Greece between the Gulf of Arta and Zakynthos, PhD thesis, Dep. Geophys., ETH, Zurich, Switzerland.

Herrmann, R.B., Malagnini, L., Munafò, I., (2011). Regional moment tensors of the 2009 L'Aquila earthquake sequence. Bull. Seismol. Soc. Am. 101. doi:10.1785/0120100184.

Hirakawa, E., A. Pitarka, and R. Mellors (2016). Generation of shear motion from an isotropic explosion source by scattering in heterogeneous media, Bulletin of the Seismological Society of America, 106, no. 5, 2313–2319, doi: 10.1785/0120150243.

Hough, S. E., Altidor, J. R., Anglade, D., Given, D., Janvier, M. G., Maharrey, J. Z., Meremonte, M., Mildor, B. S.-L., Prepetit, C., and Yong, A.: Localized damage caused by topographic amplification during the 2010 M 7.0 Haiti earthquake, Nat. Geosci., 3, 778–782, 2010.

Iervolino I, Baltzopoulos G, Chioccarelli E, Suzuki A (2019a) Seismic actions on structures in the near-source region of the 2016 central Italy sequence. Bull Earthq Eng., 17:5429–5447. https://doi.org/10.1007/s10518-017-0295-3.

Imperatori, W., and P. M. Mai (2015). The role of topogrpahy and lateral velocity heterogeneities and near-source scattering and ground-motion variability. Geophys. J. Int. (2015) 202, 2163–2181, doi: 10.1093/gji/ggv281

Lee, S.-J., Chen, H.-W., Liu, Q., Komatitsch, D., Huang, B.-S., and Tromp, J.(2008). Three-dimensional simulations of seismic-wave propagation in the Taipei basin with realistic topography based upon the spectral-element method, B. Seismol. Soc. Am., 98, 253–264.

Liberatore D, Doglioni C, AlShawa O, Atzori S, Sorrentino L., (2019). Effects of coseismic ground vertical motion on masonry constructions damage during the 2016 Amatrice-Norcia (Central Italy) earthquakes. Soil Dyn Earthq Eng 2019;120: 423–35. https://doi.org/10.1016/j.soildyn.2019.02.015

Liu, P., R. J. Archuleta, and S. H. Hartzell (2006). Prediction of broad band ground-motion time histories: Hybrid low/high-frequency method with correlated random source parameters, Bull. Seismol. Soc. Am.96,no. 6, 2118–2130, doi:10.1785/0120060036.

Ma, S., Archuleta, R.J. & Page, M.T., 2007. Effects of large-scale surface topography on ground motions, as demonstrated by a study of the San Gabriel Mountains, Los Angeles, California, Bull. seism. Soc. Am., 97(6), 2066–2079.

Magnoni, F., E. Casarotti, A. Michelini, A. Piersanti, D. Komatitsch, D. Peter, and J. Tromp (2014). Spectral-element simulations of seismic waves generated by the 2009 l'Aquila earthquake, Bull. Seismol. Soc. Am. 104, 1–22

Malagnini, L., Lucente, F. P., De Gori, P., Akinci, A. and Munafò, I., (2012), Control of pore fluid pressure diffusion on fault failure mode: Insights from the 2009 L'Aquila seismic sequence, Journal of Geophysical Research–Solid Earth, 117, B05302, doi:10.1029/2011JB008911.

Mazzoli, S., Cello, G., Deiana, G., Galdenzi, S., Gambini, R., Mancinelli, A., Mattioni, L., Shiner, P., Tondi, E., (2000). Modes of foreland deformation ahead of the Apennine thrust front. J. Czech Geol. Soc. 45, 246.

Maufroy E, Cruz-Atienza VM, Cotton F, Gaffet S (2015). Frequency-scaled curvature as a proxy for topographic site-effect amplification and ground-motion variability. Bull. Seism. Soc. Am., 105(1): 354-367. DOI: 10.1785/0120140089.

McCallen, D., N. A. Petersson, A. Rodgers, A. Pitarka, M. Miah, F. Petrone, B. Sjogreen, N. Abrahamson, H.Tang (2020a), EQSIM – A Computational Framework for Fault-to-Structure Earthquake

Simulations on Exascale Computers Part I: Computational Models and Workflow, Earthquake Spectra, 2020, https://doi.org/10.1177/8755293020970982.

McCallen, D., F. Petrone, M. Miah, A. Pitarka, A. Rodgers, N. Abrahamson (2020b), EQSIM – A Multidisciplinary Framework for Fault-to-Structure Earthquake Simulations on Exascale Computers Part II: Regional Simulations of Building Response , Earthquake Spectra, https://doi.org/10.1177/8755293020970980.

Messina, P., Galadini, F., Galli, P., Sposato, A., (2002). Quaternary basin evolution and present tectonic regime in the area of the 1997–1998 Umbria–Marche seismic sequence (central Italy). Geomorphology 42 (1-2), 97–116.

Michele, M., Chiaraluce, L., Di Stefano, R., Waldhauser, F. (2020). Fine-Scale Structure of the 2016–2017 Central Italy Seismic Sequence From Data Recorded at the Italian National Network. Journal of Geophysical Research: Solid Earth, 125(4), e2019JB018440.

Ojeda, J., Akinci, A., Tinti, E., Arriola, S, and Ruiz, S., (2021). Hybrid Broadband Strong-Motion Simulation to investigate the near-source characteristics of the M6.5, 30 October 2016 Norcia, Italy Earthquake. Submitted to Soil Dynamics and Earthquake Engineering.

Paolucci, R., I. Mazzieri, and C. Smerzini (2015). Anatomy of strong groundmotion: near-source records and 3D physics-based numerical simula-tions of the Mw6.0 May 29 2012 Po Plain earthquake, Italy,Geophys.J. Int. 203, 2001–2020.

Petersson, N. A., and B. Sjogreen (2015). Wave propagation in anisotropic elastic materials and curvilinear coordinates using a summation-by-parts finite difference method, J. Comp. Phys. 299, 820– 841, doi: 10.1016/j.jcp.2015.07.023.

Petersson, N. A., and B. E. Sjogreen (2018). SW4 Users Guide, Version 2.01, Lawrence Livermore National Laboratory, LLNL-SM–741439.

Pitarka, A. & Irikura, K., (1996). Modeling 3D surface topography by finite difference method: Kobe JMA station site, Japan, case study, Geophys. Res. Lett., 23(20), 2729–2732.

Pitarka, A., Somerville, P., Fukushima, Y., Uetake, T., & Irikura, K. (2000). Simulation of near-fault ground motion using hybrid Green's functions. Bulletin of the Seismological Society of America, 90(3), 566–586.

Pitarka A., R.J. Mellors, W.R. Walter, S. Ezzedine, O. Vorobiev, T. Antoun, J. L. Wagoner, E. M. Matzel, S. R. Ford, A. J. Rodgers, L. Glenn, and M. Pasyanos (2015). Analysis of ground motion from an underground chemical explosion. Bull. Seism. Soc. Am., 105 (5), 2390-2410, doi:10.1785/0120150066.

Pitarka A., Graves, R., Irikura, K., Miyake, H., Rodgers, A., (2017). Performance of Irikura Recipe Rupture Model Generator in Earthquake Ground Motion Simulations with Graves and Pitarka Hybrid Approach, Pure and Applied Geophysics, 174(9), doi:10.1007/s00024-017-1504-3.

Pitarka, A., R. Graves, K. Irikura, K. Miyakoshi, and A. Rodgers (2019) Kinematic rupture modeling of ground motion from the M7 Kumamoto, Japan earthquake. Pure Appl. Geophys. https://doi.org/10.1007/s00024-019-02220-5.

Pischiutta, M., Akinci, A., Tinti, E., and Herrero, A., (2021). Broadband ground-motion simulation of 2016 Amatrice earthquake, Central Italy. Geophysical Journal International, https://doi.org/10.1093/gji/ggaa412.

Pierantoni, P., Deiana, G., & Galdenzi, S. (2013). Stratigraphic and structural features of the Sibillini mountains (Umbria-Marche Apennines, Italy). Italian Journal of Geosciences, 132(3), 497-520.

Pizzi, A., Di Domenica, A., Gallovič, F., Luzi, L., Puglia, R. (2017). Fault segmentation as constraint to the occurrence of the main shocks of the 2016 Central Italy seismic sequence. Tectonics, 36(11), 2370-2387.

Rovida, A., Camassi, R., Gasperini, P., Stucchi, M. (2011). Catalogo Parametrico dei Terremoti Italiani.

Petrone, F.,N. Abrahamson,D. McCallen, A. Pitarka, and A. Rodgers (2021) Engineering Evaluation of the EQSIM Simulated Ground-Motion Database: The San Francisco Bay Area Region, submitted to the Earthquake Engineering and Structural Dynamics

Rodgers, A. J., N. A. Petersson and B. Sjogreen (2010). Simulation of topographic effects on seismic waves from shallow explosions near the North Korean nuclear test site with emphasis on shear wave generation, J. Geophys. Res.-Sol. Ea. 115, B11309, doi: 10.1029/2010JB007707.

Rodgers, A. J., A. Pitarka, N. A. Petersson, B. Sjogreen, and D.McCallen (2018). Broadband (0-4 Hz) ground motions for a magnitude 7.0 Hayward Fault earthquake with 3D structure and topography, Geophys. Res. Lett.45, 739–747.

Rossi A, Tertulliani A, Azzaro R, Graziani L, Rovida A, Maramai A, Pessina V, Hailemikael S, Buffarini G, Bernardini F, Camassi R, Del Mese S, Ercolani E, Fodarella A, Locati M, Martini G, Paciello A, Paolini S, Arcoraci L, Castellano C, Verrubbi V, Stucchi M (2019) The 2016-2017 earthquake sequence in central Italy: macroseismic survey and damage scenario through the EMS-98 intensity assessment. Bull Earthq Eng 17:2407–2431. https://doi.org/10.1007/s10518-019-00556-w.

Scisciani, V., Agostini, S., Calamita, F., Pace, P., Cilli, A., Giori, I., & Paltrinieri, W., (2014). Positive inversion tectonics in foreland fold-and-thrust belts: A reappraisal of the Umbria–Marche Northern Apennines (Central Italy) by integrating geological and geophysical data. Tectonophysics, 637, 218-237.

Scognamiglio, L., Tinti, E., Casarotti, E., Pucci, S., Villani, F., Cocco, M., Dreger, D. (2018). Complex fault geometry and rupture dynamics of the Mw 6.5, 30 October 2016, Central Italy earthquake. Journal of Geophysical Research: Solid Earth, 123(4), 2943-2964.

Shafique, M., van der Meijde, M., Kerle, N., and van der Meer, F. 2011. Impact of DEM source and resolution on topographic seismic amplification, Int. J. Appl. Earth Obs., 13, 420–427.

Sjogreen, B., and N. A. Petersson (2012). A fourth order accurate finite difference method for the elastic wave equation in second order formulation, J. Sci. Comput. 52, no. 1, 17–48, doi:10.1007/s10915-011-9531-1.

Sjogreen, B., and N. A. Petersson (2015), Spectral and high order methods for partial differential equations ICOSAHOM 2014, in Selected Papers From the ICOSAHOM Conference, June 23–27, 2014, Salt Lake City, Utah, USA, chap. Summation by Parts Finite Difference Approximations for Seismic and Seismo-Acoustic Computations, pp. 455– 463, Springer Int. Publ., Switzerland, doi:10.1007/978-3-319-19800-2-42.

Spudich, P., Hellweg, M. & Lee, W.H.K., 1996. Directional topographic site response at Tarzana observed in aftershocks of the 1994 Northridge, California, earthquake: implications for mainshock motions, Bull. seism. Soc. Am., 86(1), S193–S208.

Stucchi, M., Camassi, R., Rovida, A., Locati, M., Ercolani, E., Meletti, C., Migliavacca, P., Bernardini, F., Azzaro, R., (2007). DBMI04, il database delle osservazioni macrosismiche dei terremoti italiani utilizzate per la compilazione del catalogo parametrico CPTI04. In: Quaderni di Geofisica.

Taborda, R., and J. Bielak (2013). Ground-motion simulation and validation of the 2008 Chino Hills, California, earthquake, Bull.Seismol. Soc. Am.103,no. 1, 131–156.

Tinti E, Scognamiglio L, Michelini A, Cocco M (2016). Slip heterogeneity and directivity of the ML 6.0, 2016, Amatrice earthquake estimated with rapid finite-fault inversion. Geophys. Res. Lett. 43(20): 10,745-10,752.

Villani, F., Pucci, S., Civico, R., De Martini, P. M., Cinti, F. R., Pantosti, D. (2018). Surface faulting of the 30 October 2016 Mw 6.5 central Italy earthquake: Detailed analysis of a complex coseismic rupture. Tectonics, 37(10), 3378-3410.

Villani, F., Civico, R., Pucci, S., Pizzimenti, L., Nappi, R., De Martini, P. M., and The Open EMERGEO Working Group (2018). A database of the coseismic effects following the 30 October 2016 Norcia earthquake in central Italy. Scientific Data, 5, 180,049.

Wang, S., and N. A. Petersson (2019). Fourth order finite difference methods for the wave equation with mesh refinement interfaces, J. Sci. Comput. 41, no. 5, A3246–A3275.

Wessel, P., Smith, W. H., Scharroo, R., Luis, J., & Wobbe, F. (2013). Generic mapping tools: improved version released. Eos, Transactions American Geophysical Union, 94(45), 659 409-410.

Authors:

Arben Pitarka
Lawrence Livermore National Laboratory
7000 East Avenue
Livermore, CA 94550, USA

Aybige Akinci
Istituto Nazionale di Geofisica e Vulcanologia
via di Vigna Murata 60500143, Rome, Italy

Pasquale De Gori
Istituto Nazionale di Geofisica e Vulcanologia
via di Vigna Murata 60500143, Rome, Italy

Mauro Buttinelli

Istituto Nazionale di Geofisica e Vulcanologia

via di Vigna Murata 60500143, Rome, Italy

Table 1 Strong motion stations used in this study, and corresponding PGV and PGA recorded the M_w6.5 Norcia earthquake. The last column indicates the site classification according to EC-18 and NTC18 (CEN, 2004).

No.	Station Code	Lat (°)	Lon (°)	R_{jb} (km)	PGA_N (cm/s²)	PGA_E (cm/s²)	PGA_Z (cm/s²)	PGV_N (cm/s)	PGV_E (cm/s)	PGV_Z (cm/s)	EC8
1	ACC	42.696	13.242	0.00	387.15	456.00	561.14	38.50	42.15	21.63	A
2	FCC	42.755	13.193	0.00	847.80	1008.31	841.37	44.83	69.25	52.75	A
3	CLO	42.829	13.206	0.00	614.99	406.93	744.12	52.93	60.70	73.40	B
4	CNE	42.894	13.153	0.00	302.91	433.14	586.12	23.90	42.05	17.82	B
5	T1214	42.760	13.209	0.00	431.99	665.85	618.15	73.10	24.43	14.83	B
6	T1201	42.657	13.251	1.00	467.79	355.83	224.24	41.38	54.99	27.28	B
7	NRC	42.793	13.096	1.21	324.51	441.99	365.02	38.24	45.24	21.56	B
8	NOR	42.792	13.092	1.52	312.78	307.61	271.52	43.23	52.99	25.77	B
9	T1299	42.634	13.282	1.72	466.39	450.27	313.68	27.99	23.01	23.07	B
10	T1244	42.757	13.298	1.78	188.33	278.34	339.17	27.10	21.64	18.96	A
11	PRE	42.879	13.033	1.81	310.95	257.24	200.00	15.96	11.19	6.72	B
12	AMT	42.632	13.286	2.04	425.43	565.02	322.51	31.21	29.48	31.78	B
13	T1213	42.725	13.126	2.22	874.74	802.73	828.15	33.54	49.62	30.29	B
14	T1216	42.891	13.019	2.34	264.21	256.49	161.91	13.28	13.62	6.48	A
15	CIT	42.594	13.163	5.83	211.92	333.05	140.86	14.34	16.51	8.99	B
16	T1212	42.752	13.045	6.97	252.60	269.73	166.05	24.01	24.65	12.70	B
17	MCV	42.993	13.001	9.63	365.42	307.65	433.39	11.27	7.43	6.73	B
18	MMO	42.899	13.327	10.60	192.27	194.03	143.57	13.93	10.88	10.49	B
19	CSC	42.719	13.012	10.89	155.07	160.18	161.47	10.48	11.70	6.04	A
20	ACT	42.771	13.413	10.93	386.88	257.26	260.03	10.40	5.27	6.38	C
21	PCB	42.558	13.338	11.32	241.76	138.04	59.12	9.00	9.28	8.21	B
22	MNF	43.060	13.184	12.55	114.64	126.19	106.50	7.00	7.00	6.06	A
23	MSC	42.527	13.351	14.91	95.58	93.81	49.32	9.21	8.15	8.26	B
24	MSCT	42.527	13.351	14.92	99.06	98.02	51.78	9.46	8.49	8.52	B
25	T1219	43.056	13.005	15.79	264.57	156.21	145.76	9.73	6.14	6.81	B
26	SNO	43.037	13.304	15.81	115.66	80.75	70.73	6.46	6.60	5.29	B
27	SPD	42.515	13.371	16.78	106.00	77.68	47.53	7.80	6.72	7.33	A
28	CLF	43.037	12.920	17.00	164.81	114.86	94.79	9.82	10.70	5.75	B
29	T1217	42.712	12.931	17.22	111.26	107.68	93.16	7.87	4.19	5.33	B
30	FOC	43.026	12.897	17.30	333.05	370.75	224.58	7.18	12.20	4.84	C
31	T1215	42.802	12.869	17.64	85.84	76.19	64.05	4.68	6.99	4.52	A
32	T1220	43.110	13.089	18.59	258.52	234.42	142.52	15.69	16.33	7.79	B
33	FOS	43.015	12.835	20.21	119.21	83.97	50.94	6.06	5.31	2.85	C
34	LSS	42.558	12.969	21.65	53.05	44.44	41.03	3.73	3.96	3.70	A
35	TERO	42.623	13.604	22.88	122.23	87.49	57.19	8.58	6.20	3.66	B
36	PZI1	42.436	13.326	23.26	58.00	68.88	30.30	6.93	5.82	5.24	A
37	TRE	42.877	12.736	24.96	122.42	120.71	65.71	8.71	6.65	4.50	C
38	ANT	42.418	13.079	25.99	49.25	41.59	23.91	6.10	6.54	2.63	A
39	MDAR	43.193	13.143	27.05	69.81	88.08	58.99	4.22	4.49	2.62	B
40	FOPC	42.970	12.703	28.12	93.00	114.08	51.38	4.98	6.90	3.03	B
41	TRL	42.461	12.932	29.76	97.32	70.69	32.51	7.85	8.23	2.59	B

Table 2. Fault Segment Parameters for the Kinematic Rupture Model of the M_w6.5 October 30th 2016, Norcia Italy earthquake.

Segment	Top center Longitude	Top center Latitude	Length (km)	Strike	Dip	Average Rake
1	13.21	42.86	26	152	40	-90
2	13.18	42.78	10	210	45	-30

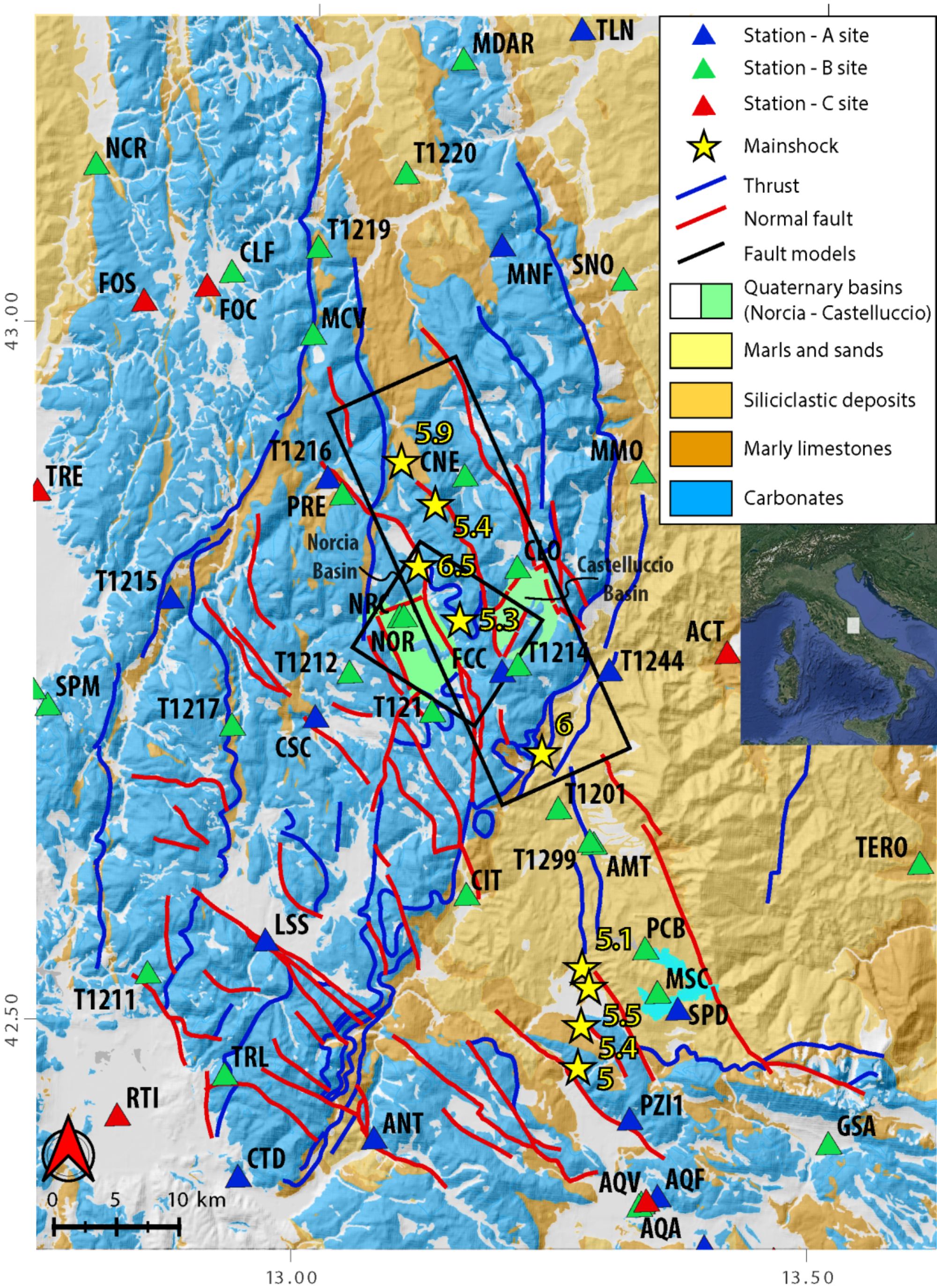

Figure 1. Geological map of the Norcia region**.** Yellow stars indicate the epicenter of seismic events with a magnitude larger than 5.0 (INGV catalog, ISIDE 2016) that occurred during the 2016-2017 earthquake sequence. Triangles with different colors indicate the location of strong motion stations considered in this study. The color scheme of the geological units is based on the NTC-18 V_{s30}site classification. The black rectangles indicate the surface projection of the two segment fault model of the October 30th, 2016 M6.5 Norcia earthquake (Scognamiglio et al.,2018).

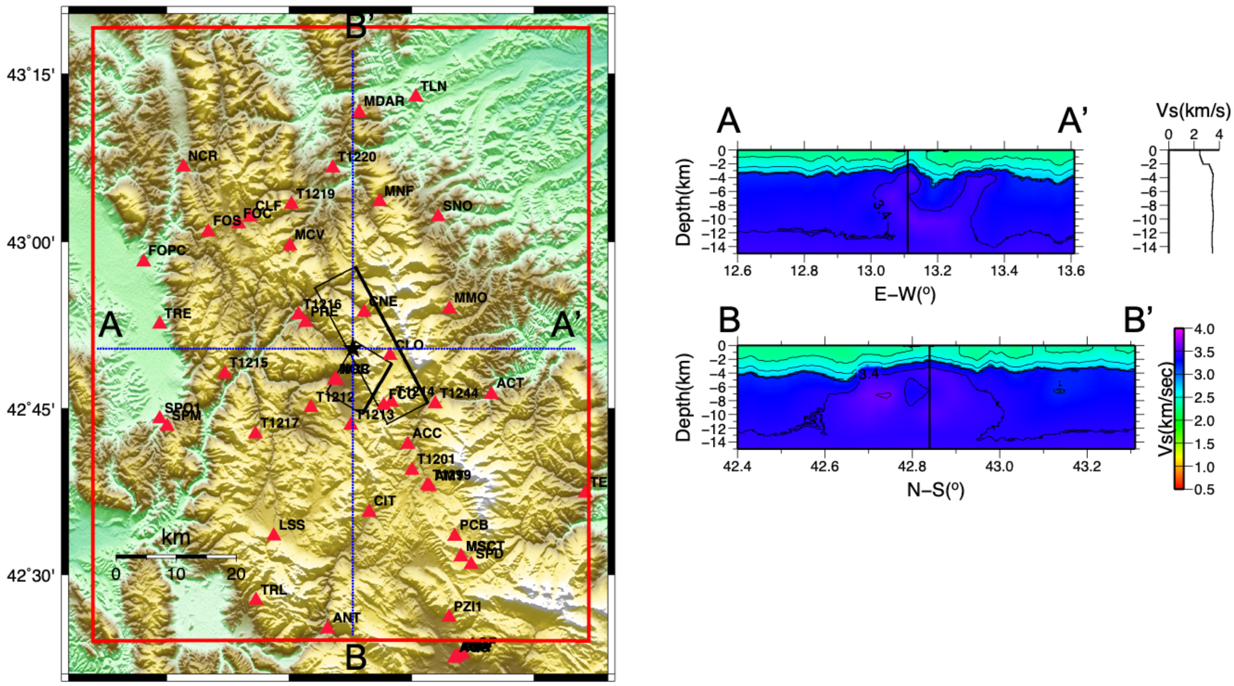

Figure 2. Topography map showing the study area indicated by the red rectangle (top panel), and vertical cross sections of the 3D velocity model used in the simulations (left panels) along A-A' and B-B' lines, indicated by dotted lines on the map. The black star indicates the epicenter of the Norcia M_w6.5 30th October 2016 earthquake. The surface projection of the causative fault with its secondary fault segment is showed by the black rectangles. Red triangles indicate the strong motion stations used in this study. The 1D Vs profile shown next to the velocity cross section A-A' presents the shear-wave velocity extracted from the 3D model at the epicenter, along the vertical black line indicated in both vertical cross sections.

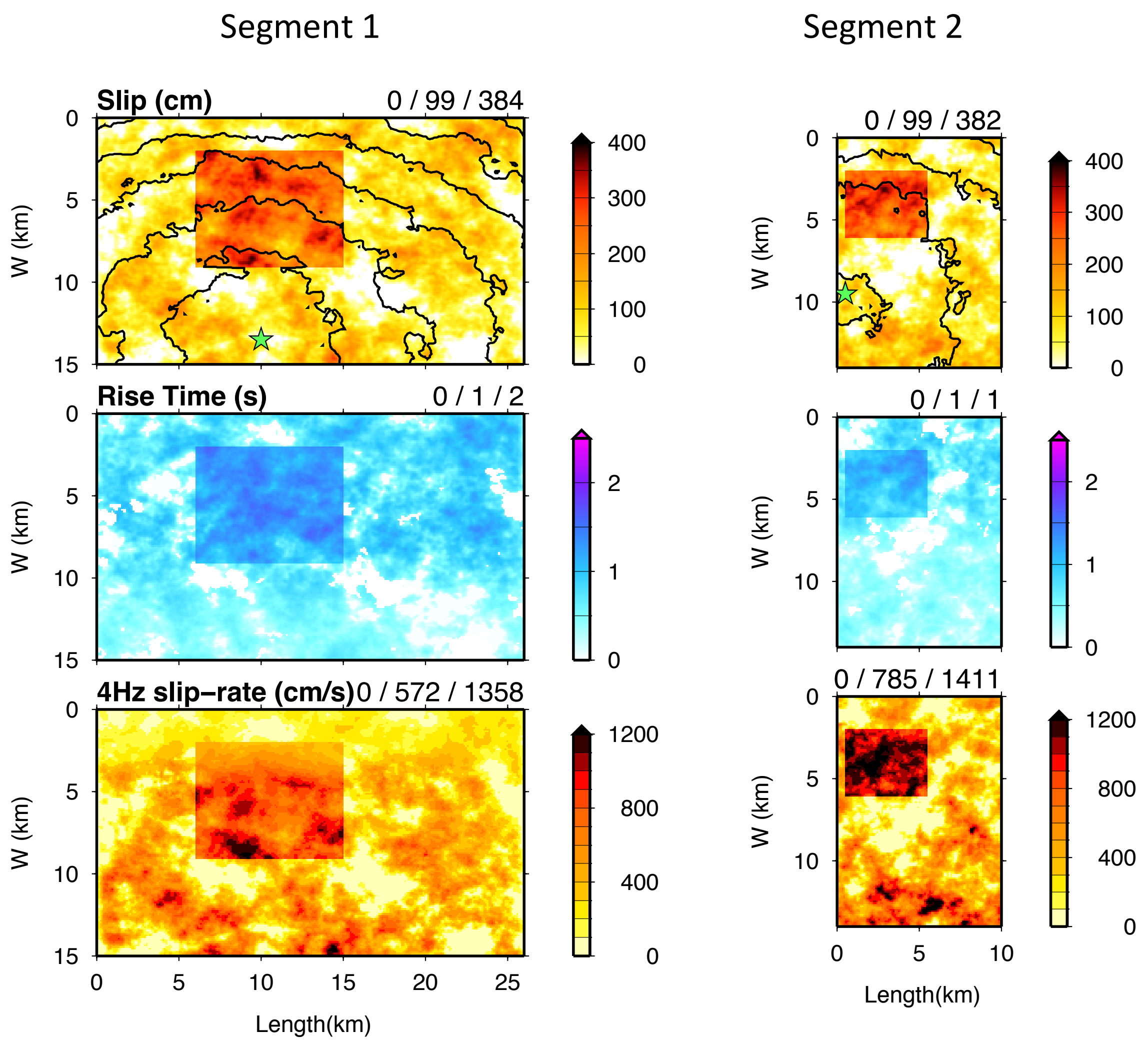

Figure 3. Kinematic rupture model for the M_w6.5 Norcia earthquake adopted from Scognamiglio et al., (2018) using a hybrid approach (Pitarka et al., 2019) that combines deterministic large slip patches with rectangular shape, with random perturbations (Model 1). Left panel shows the main fault rupture model, and the right panel shows the secondary fault model activated during the Norcia earthquake. Top panels: Slip distribution and rupture time contours at 2 s. Middle panels: rise time. Bottom panels: peak slip rate computed from the slip rate function low pass filtered at 4 Hz.

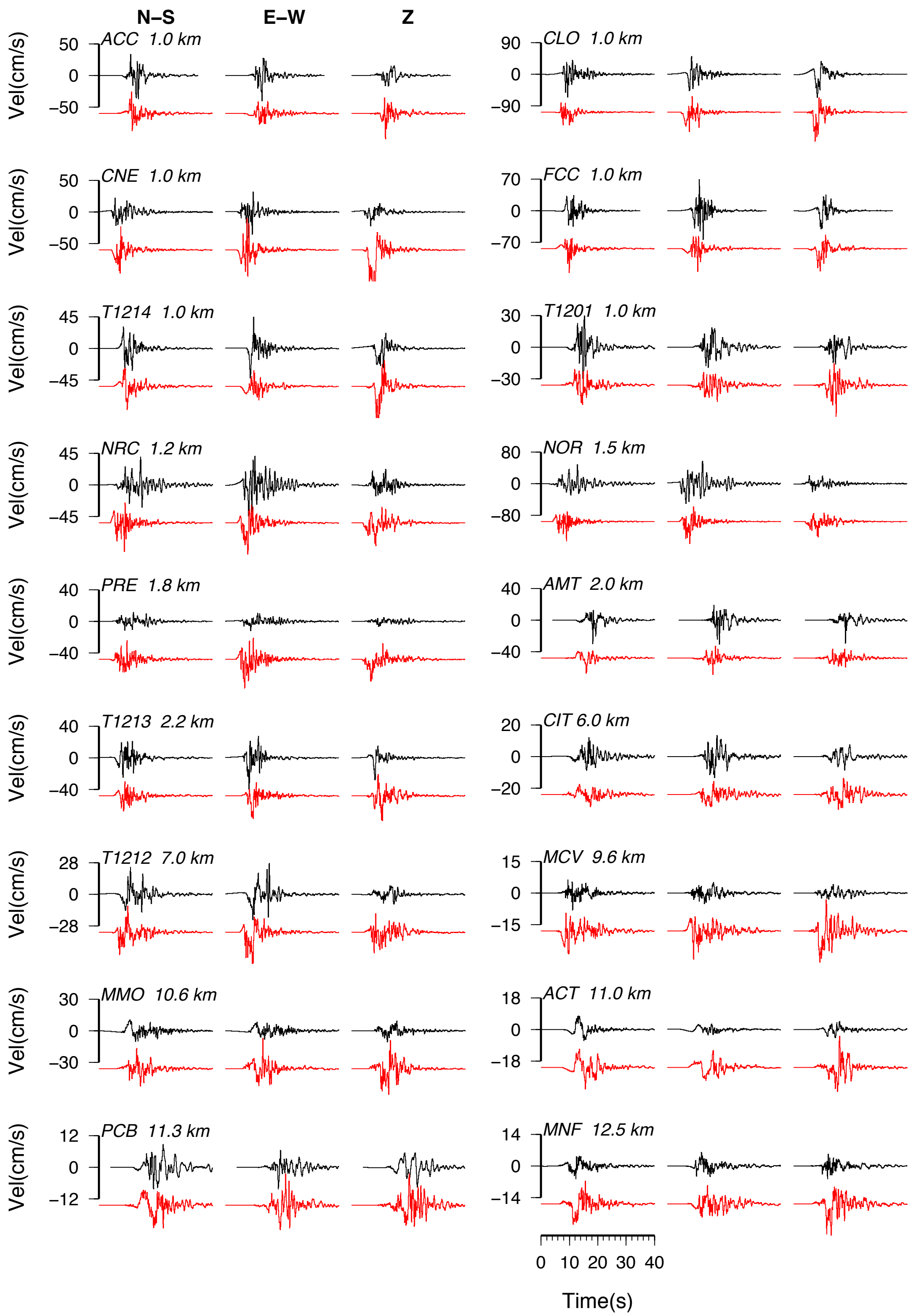
N–S
E–W
Z
Vel(cm/s)
ACC 1.0 km
CLO 1.0 km
CNE 1.0 km
FCC 1.0 km
T1214 1.0 km
T1201 1.0 km
NRC 1.2 km
NOR 1.5 km
PRE 1.8 km
AMT 2.0 km
T1213 2.2 km
CIT 6.0 km
T1212 7.0 km
MCV 9.6 km
MMO 10.6 km
ACT 11.0 km
PCB 11.3 km
MNF 12.5 km
0 10 20 30 40
Time(s)

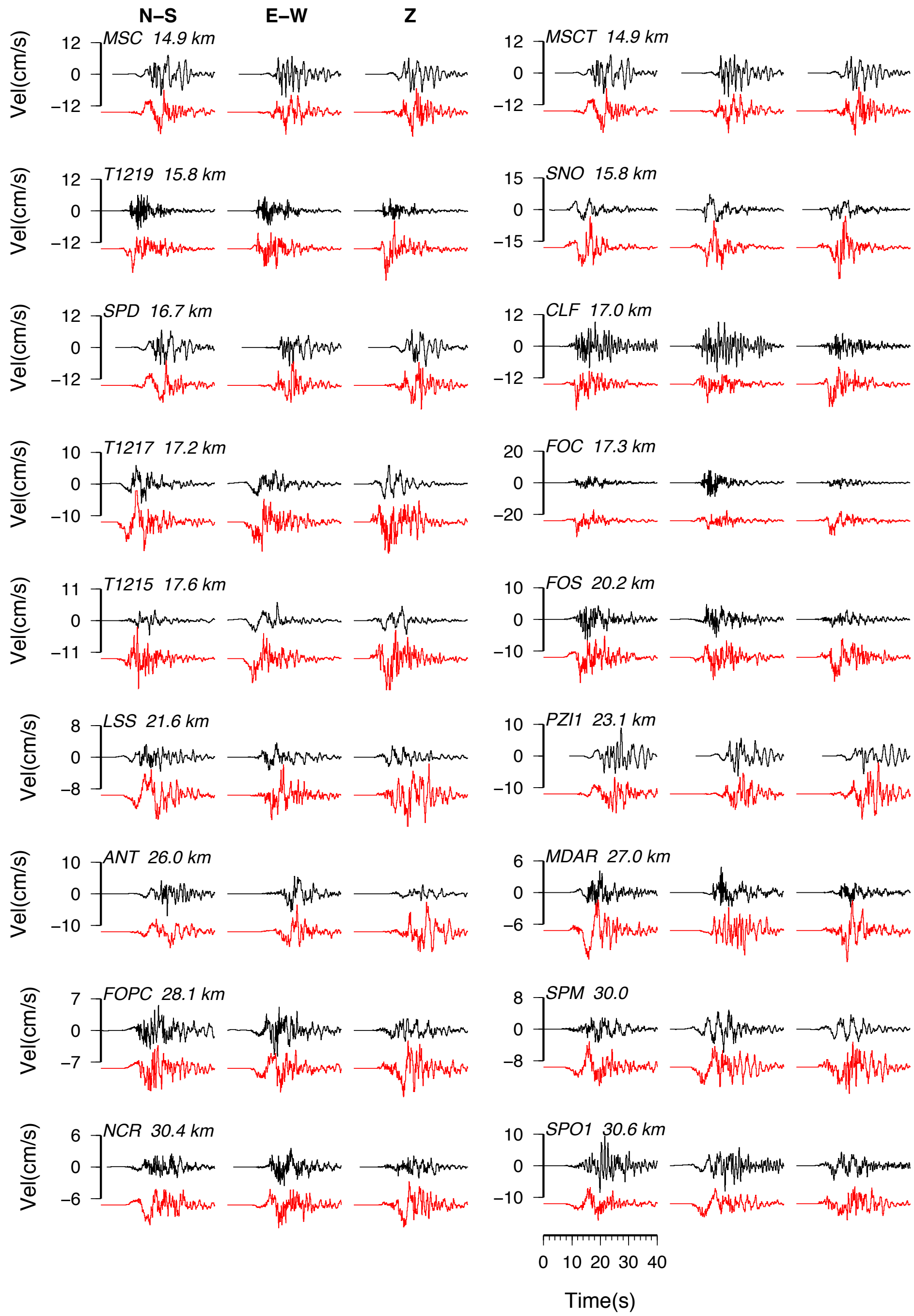

Figure 4. Comparison of recorded (black traces) and simulated (red traces) three-component time histories of ground motion velocity of the 2016 Norcia earthquake, low pass-filtered at 5Hz. The station's name and its closest distance to the fault are indicated in each panel.

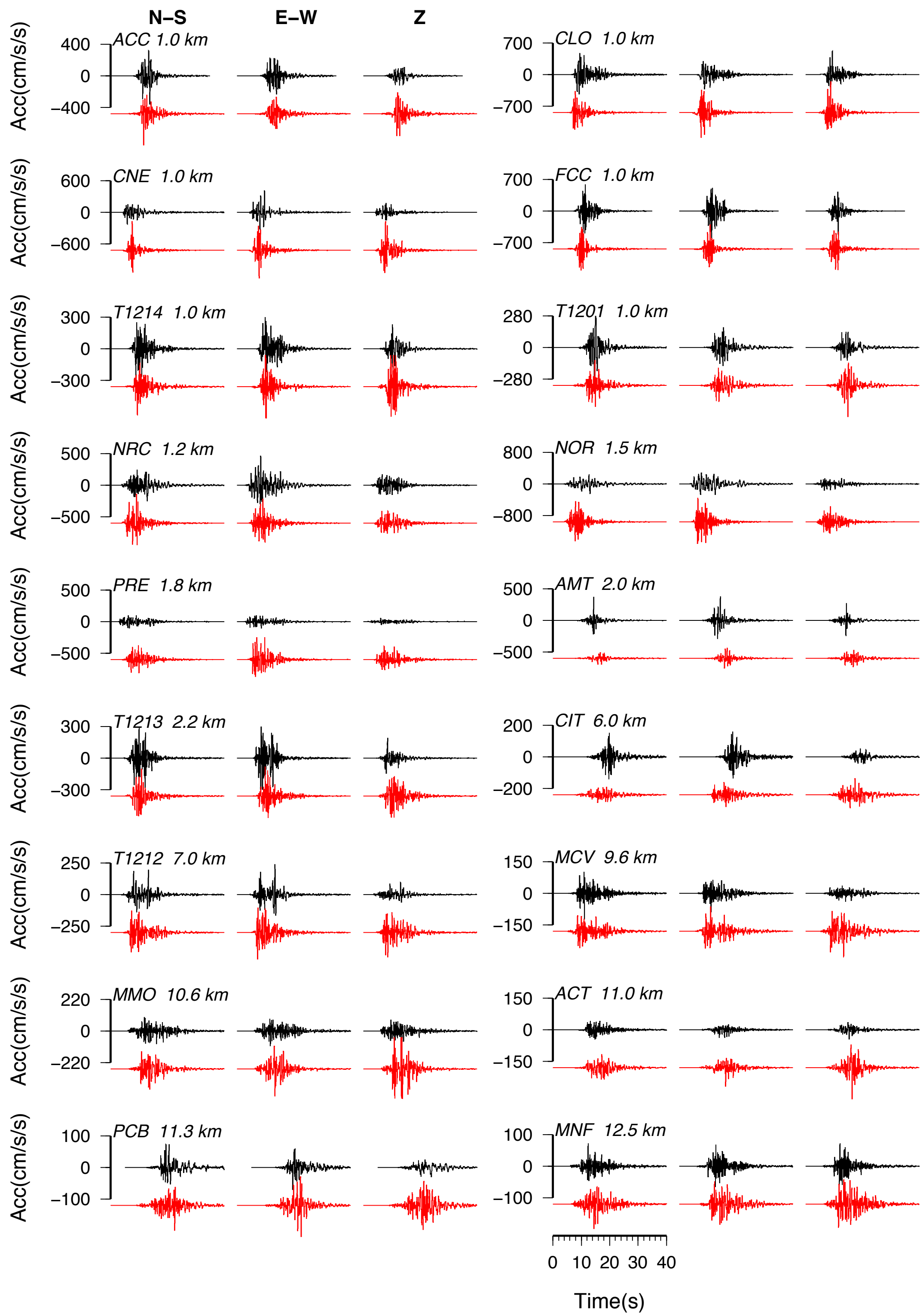
N–S
E–W
Z
Acc(cm/s/s)
ACC 1.0 km
400
0
–400
CLO 1.0 km
700
0
–700
CNE 1.0 km
600
0
–600
FCC 1.0 km
700
0
–700
T1214 1.0 km
300
0
–300
T1201 1.0 km
280
0
–280
NRC 1.2 km
500
0
–500
NOR 1.5 km
800
0
–800
PRE 1.8 km
500
0
–500
AMT 2.0 km
500
0
–500
T1213 2.2 km
300
0
–300
CIT 6.0 km
200
0
–200
T1212 7.0 km
250
0
–250
MCV 9.6 km
150
0
–150
MMO 10.6 km
220
0
–220
ACT 11.0 km
150
0
–150
PCB 11.3 km
100
0
–100
MNF 12.5 km
100
0
–100
0 10 20 30 40
Time(s)

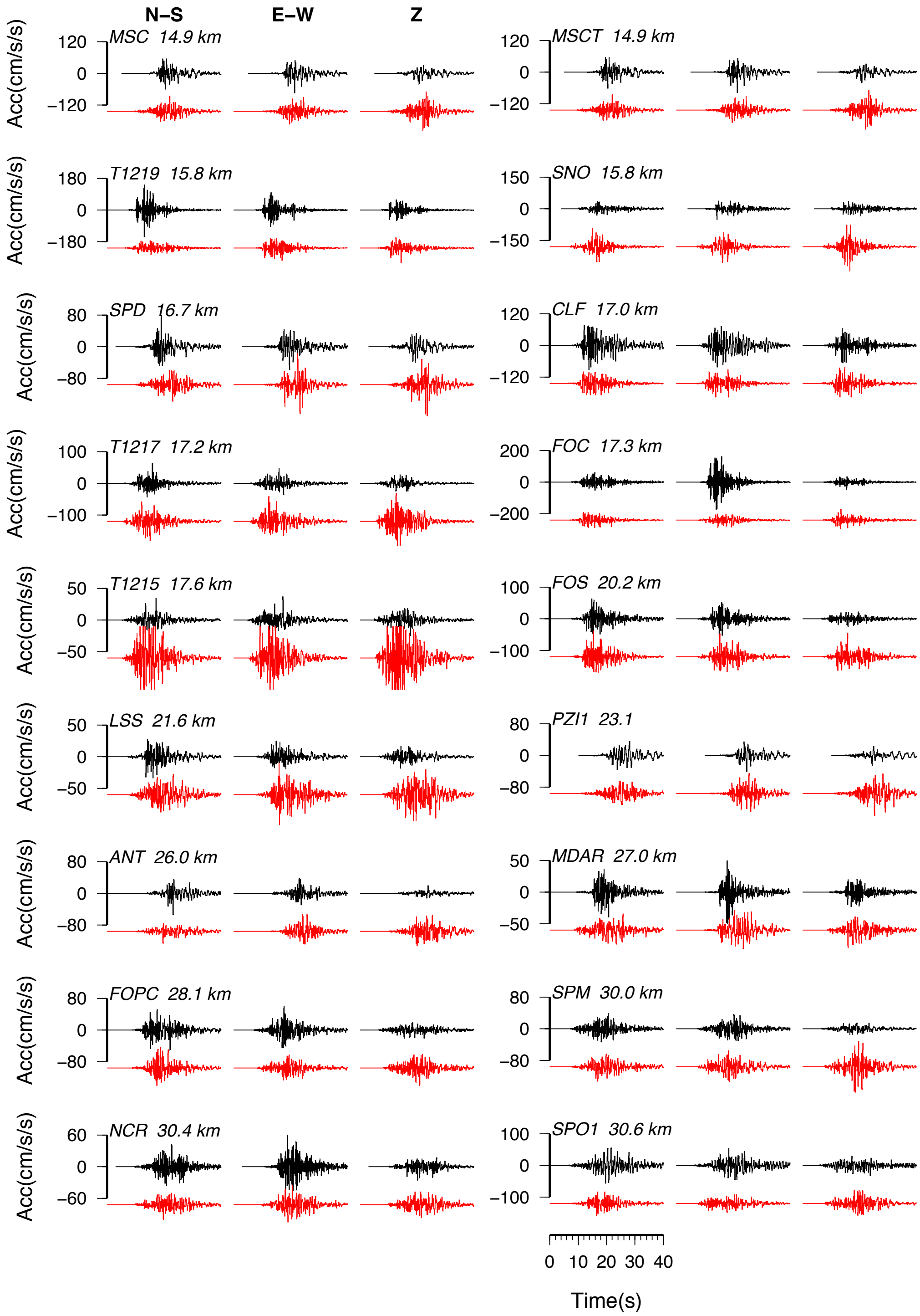

Figure 5. Comparison of recorded (black traces) and simulated (red traces) three-component time histories of ground motion acceleration of the 2016 Norcia earthquake, low pass-filtered at 5Hz. The station's name and its closest distance to the fault are indicated in each panel.

1016

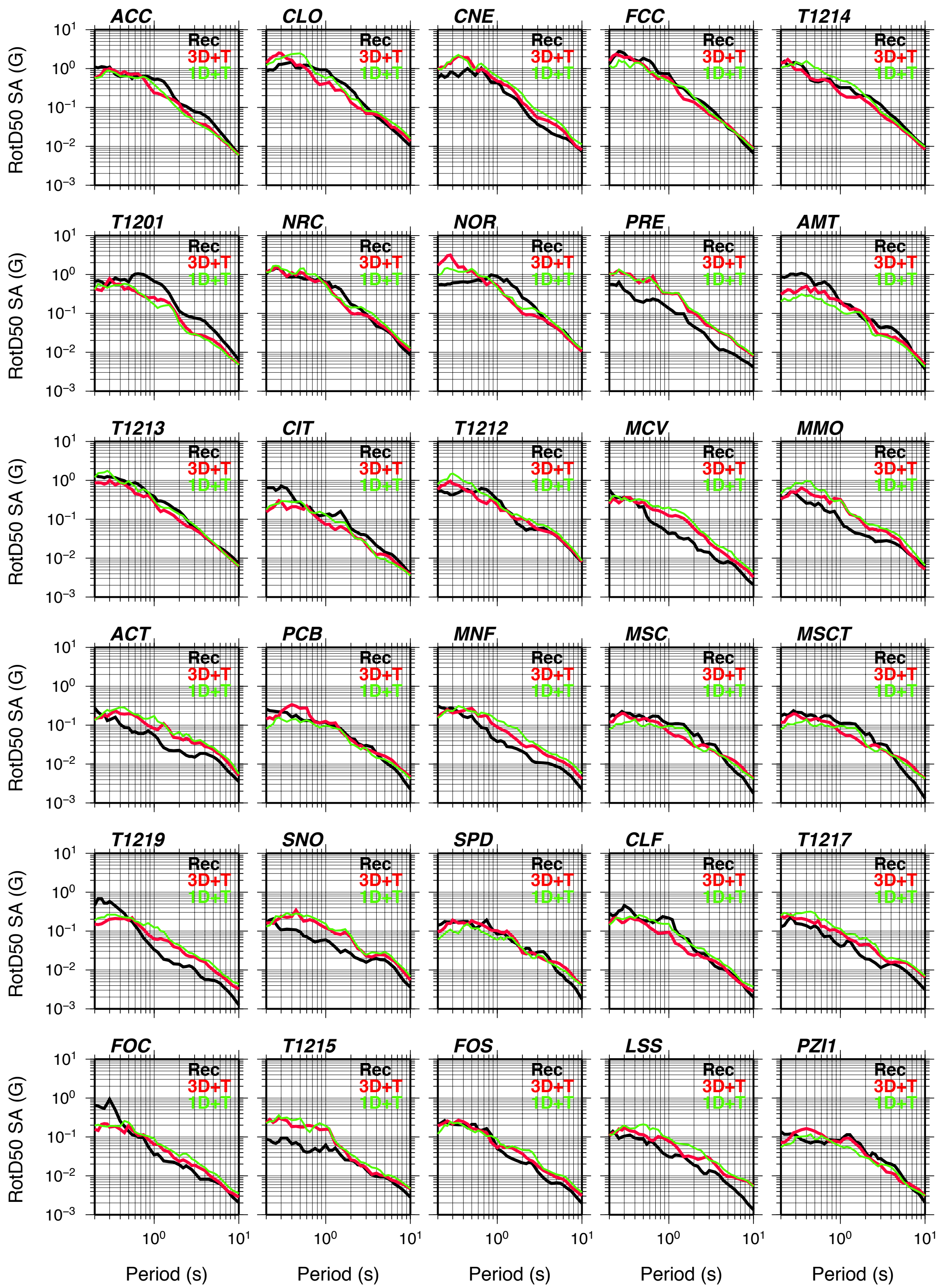

ACC
CLO
CNE
FCC
T1214
T1201
NRC
NOR
PRE
AMT
T1213
CIT
T1212
MCV
MMO
ACT
PCB
MNF
MSC
MSCT
T1219
SNO
SPD
CLF
T1217
FOC
T1215
FOS
LSS
PZI1
Rec
3D+T
1D+T
RotD50 SA (G)
Period (s)

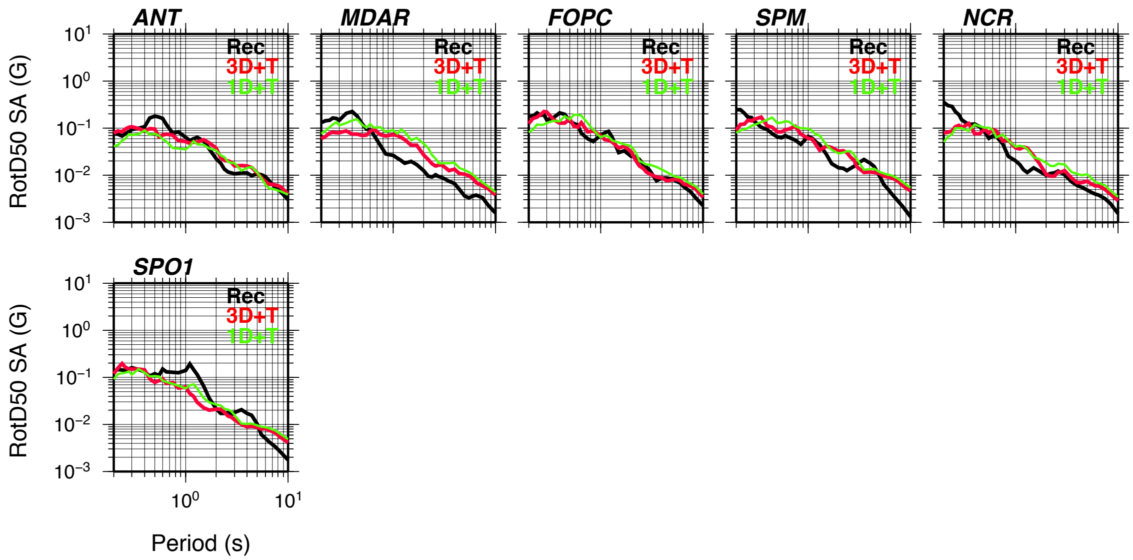

Figure 6. Comparison of recorded (black traces) and simulated 5% damped RotD50 pseudo spectral acceleration of the 2016 Norcia earthquake, using the 3D model (red traces) and 1D model (green traces).

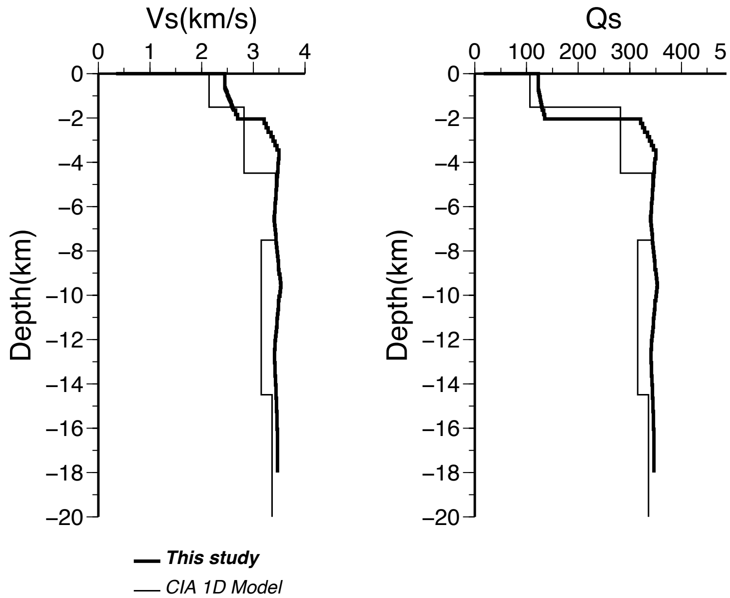

Figure 7. 1D velocity, V_s models and 1D quality factor, Q_s models of the Central Italian Apennine (CIA) region (thin line) and the corresponding 1D profile obtained from the local 3D model at the earthquake epicenter location.

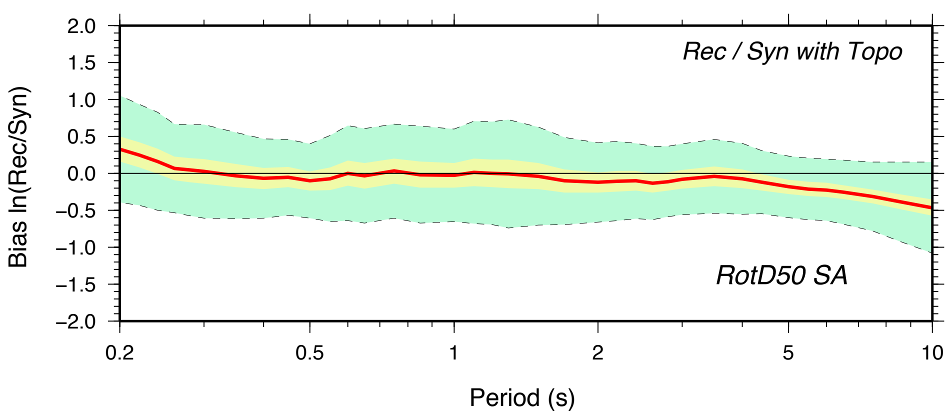

Figure 8. Norcia earthquake goodness-of-fit plot showing the model bias (solid line) and standard deviation (dashed lines) of residuals between the recorded and simulated RotD50 spectral acceleration values in the period range 0.2 to 10 s, averaged over 41 stations. The synthetic ground motion was computed using a 3D velocity model with topography and source Model 1.

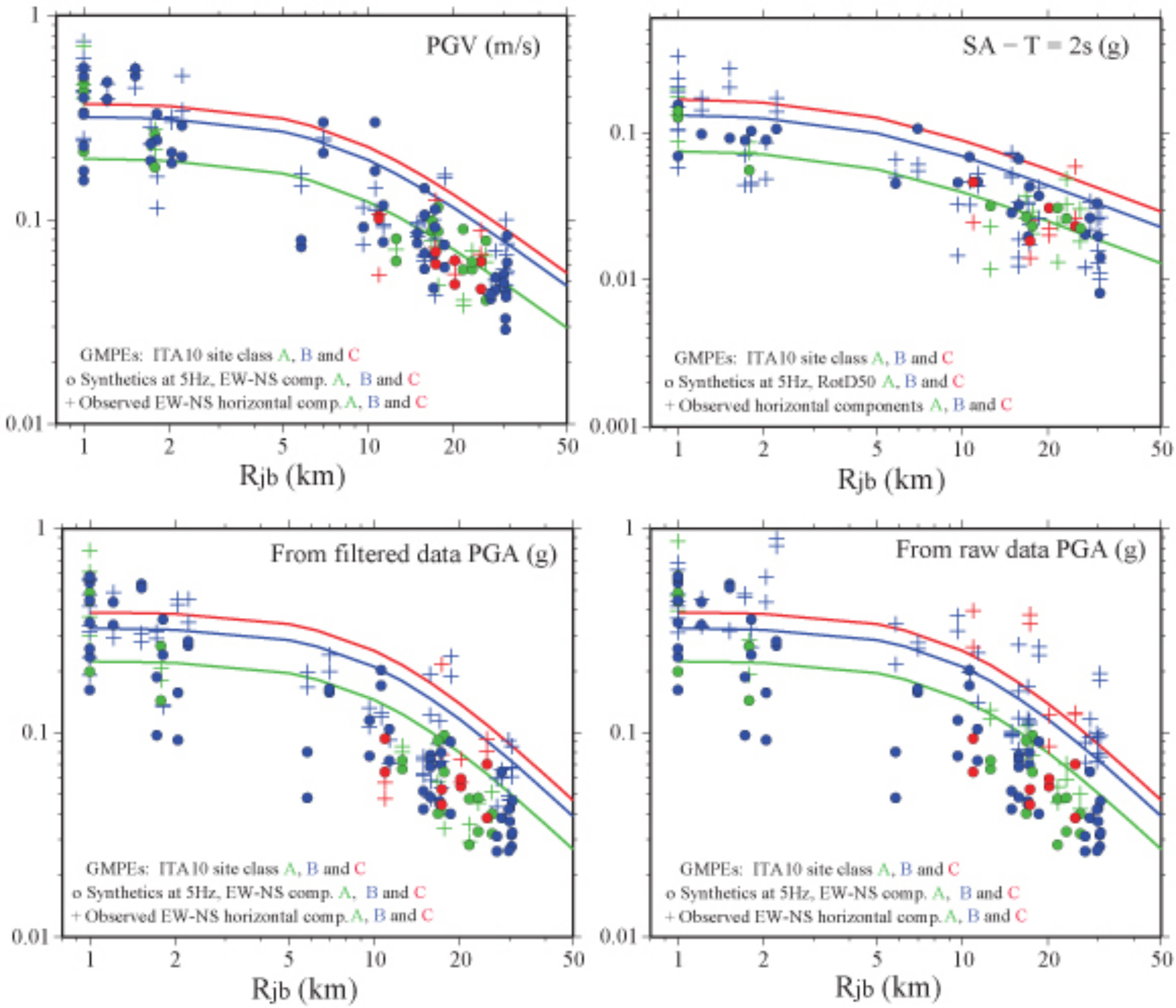

Figure 9. Comparison of recorded (crosses) and simulated (circles) ground motion with M_w6.5 Central Italy GMMs (Bindi et al., 2011) generated for a normal faulting M_w6.5 earthquake, for three different site conditions rock (green), hard soil (blue), and soft soil (red) type, for the PGV (top left panel), SA2.0s (top right panel), PGA low-passed at 5Hz (bottom left panel, and PGA using unfiltered raw recorded data (bottom right panel).

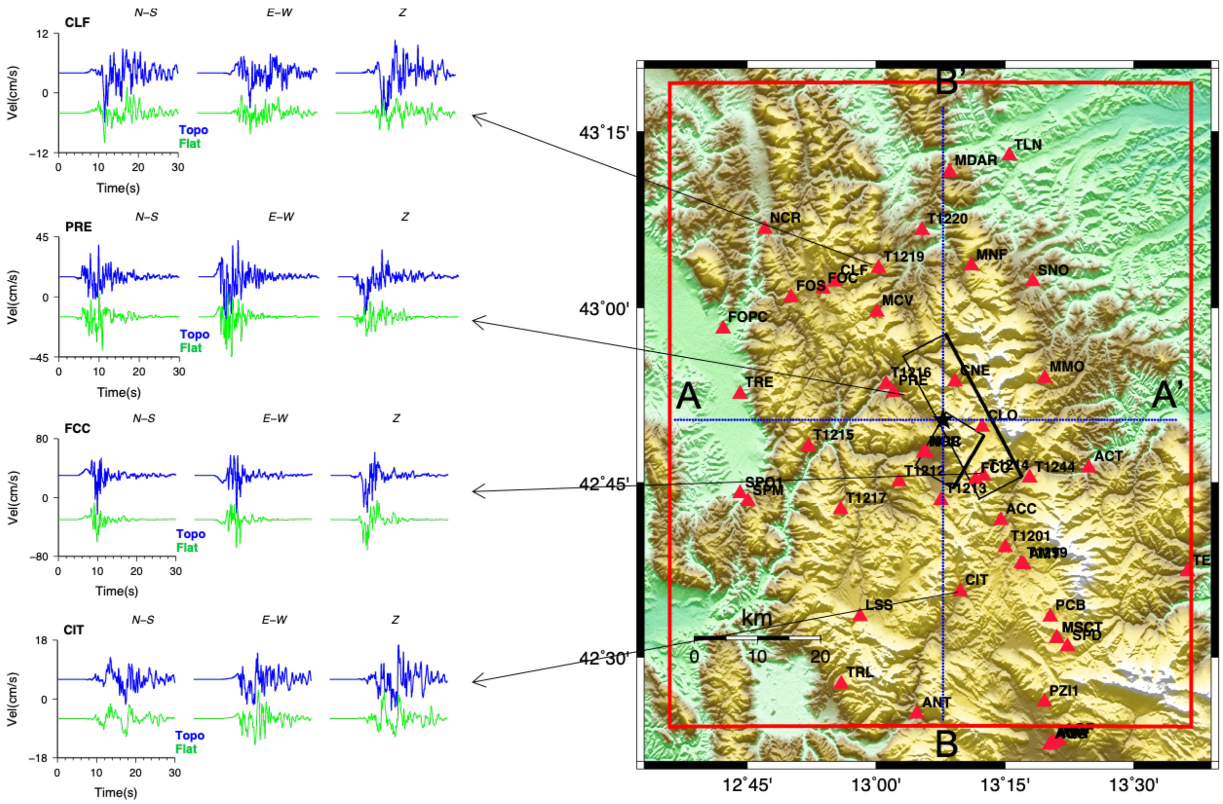

Figure 10. Waveform comparison illustrating topography effects on time histories of ground motion velocity computed at four selected strong motion stations, CLF, PRE, FCC, and CIT, located in the near source region. Blue traces are seismograms computed with surface topography and green traces are seismograms computed using with flat free surface and using rupture Model 1.

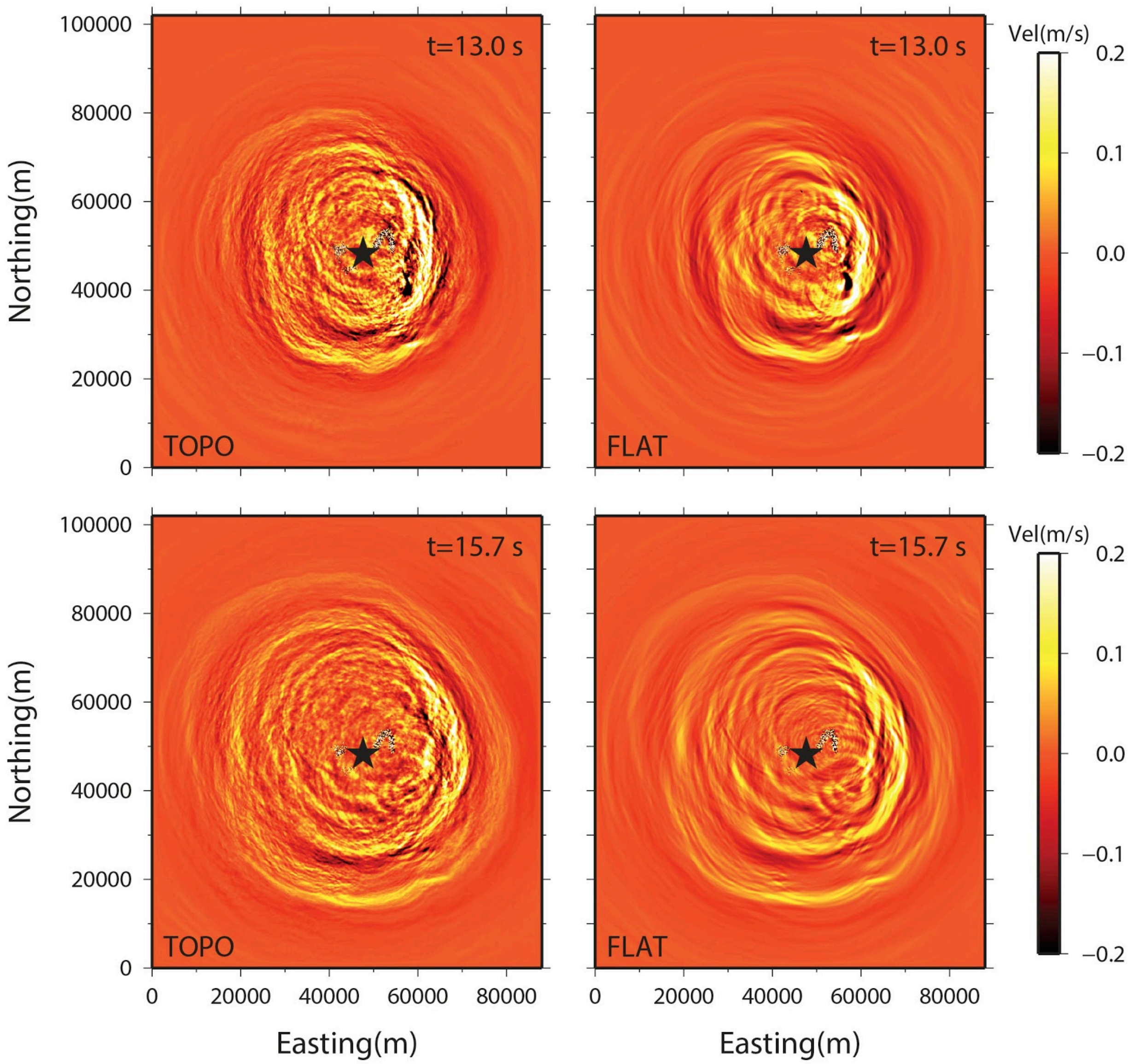

Figure 11. Snapshots of the vertical component of M_w6.5 Norcia earthquake wave fields computed with surface topography (TOPO) and with flat free surface (FLAT), at 13.0s and 15.7s into the earthquake. Star indicates the epicenter of the earthquake.

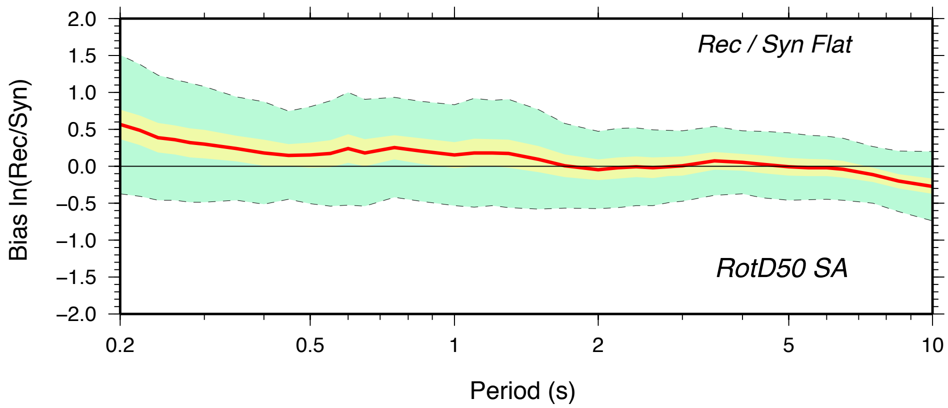

Figure 12. Norcia earthquake goodness-of-fit (GoF) plot showing the model bias (solid line) and standard deviation (dashed lines) of residuals between the recorded and simulated RotD50 spectral acceleration values in the period range 0.2 to 10 s, averaged over 41 stations. The synthetic ground motion was computed using a 3D velocity model with flat free surface and source Model 1.

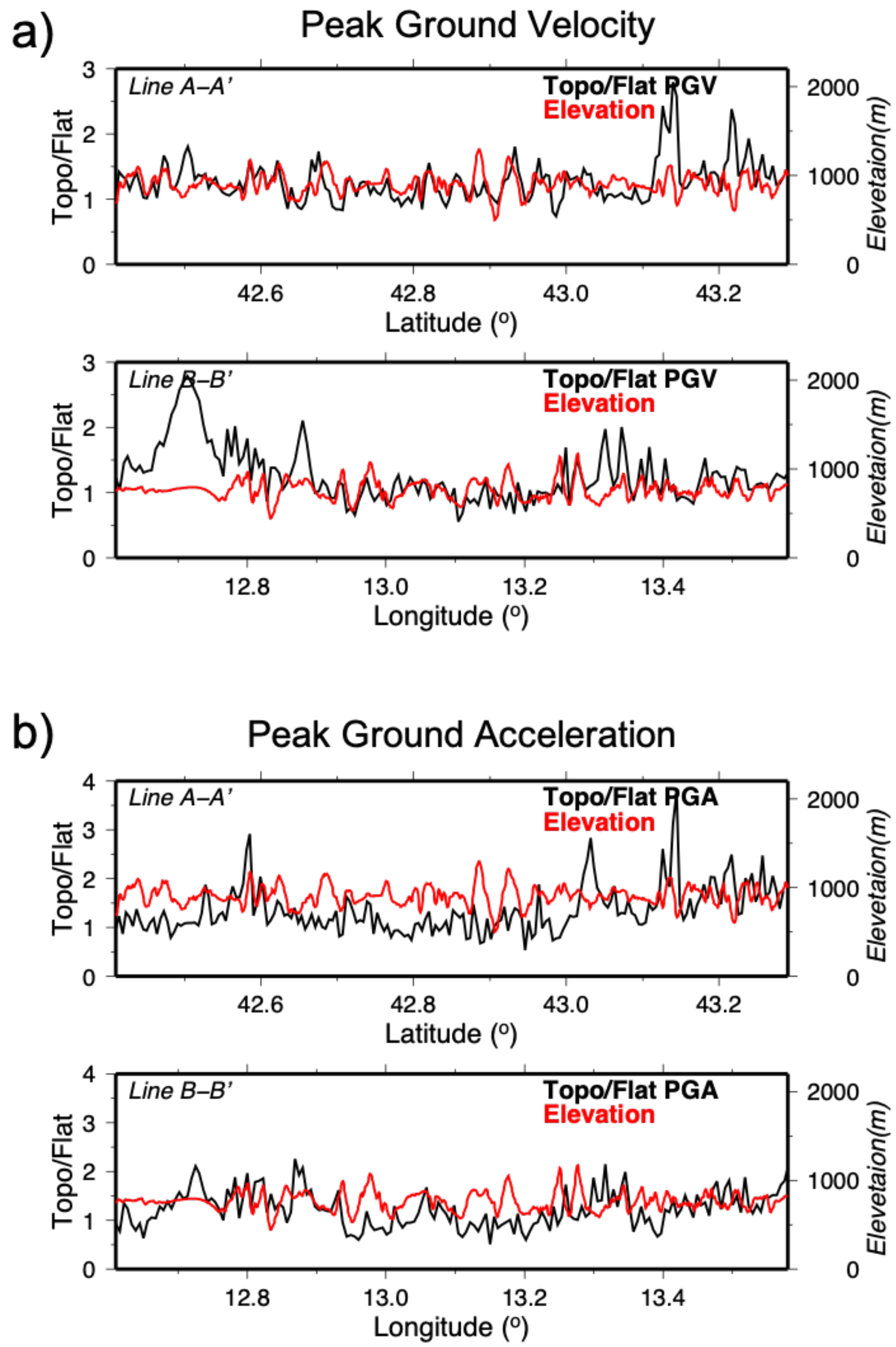

Figure 13. Ratio (black traces) between ground motions obtained with and without topography (Topo/Flat), for PGV (a) and PGA (b) along Line A-A' and Line B-B' indicated in **Figure 10**. In each panel the red trace is the ground surface elevation, high-pass filtered at elevation variations lengths of 10 km. This filter removes ground elevation variations with lengths longer than 10 km.

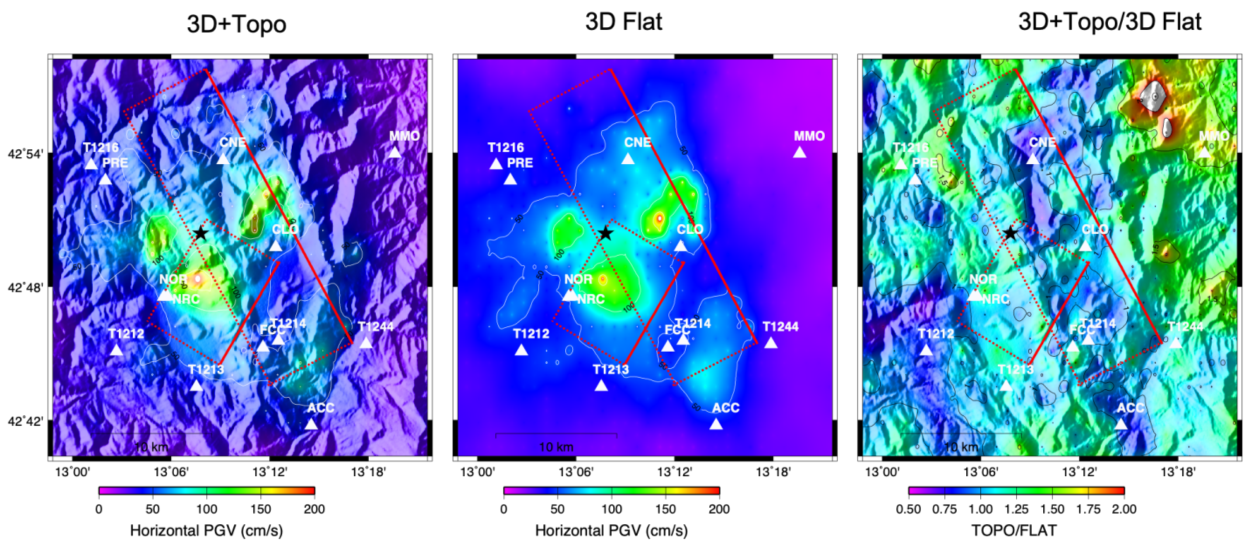

Figure 14. Maps of simulated horizontal PGV for Norcia earthquake, computed with the reginal 3D model and surface topography (left panel), computed with the reginal 3D model and flat earth surface (middle panel) and their respective ratio (right panel). Red rectangles indicate the free surface fault projection, and the star indicates the location of the rupture initiation point.

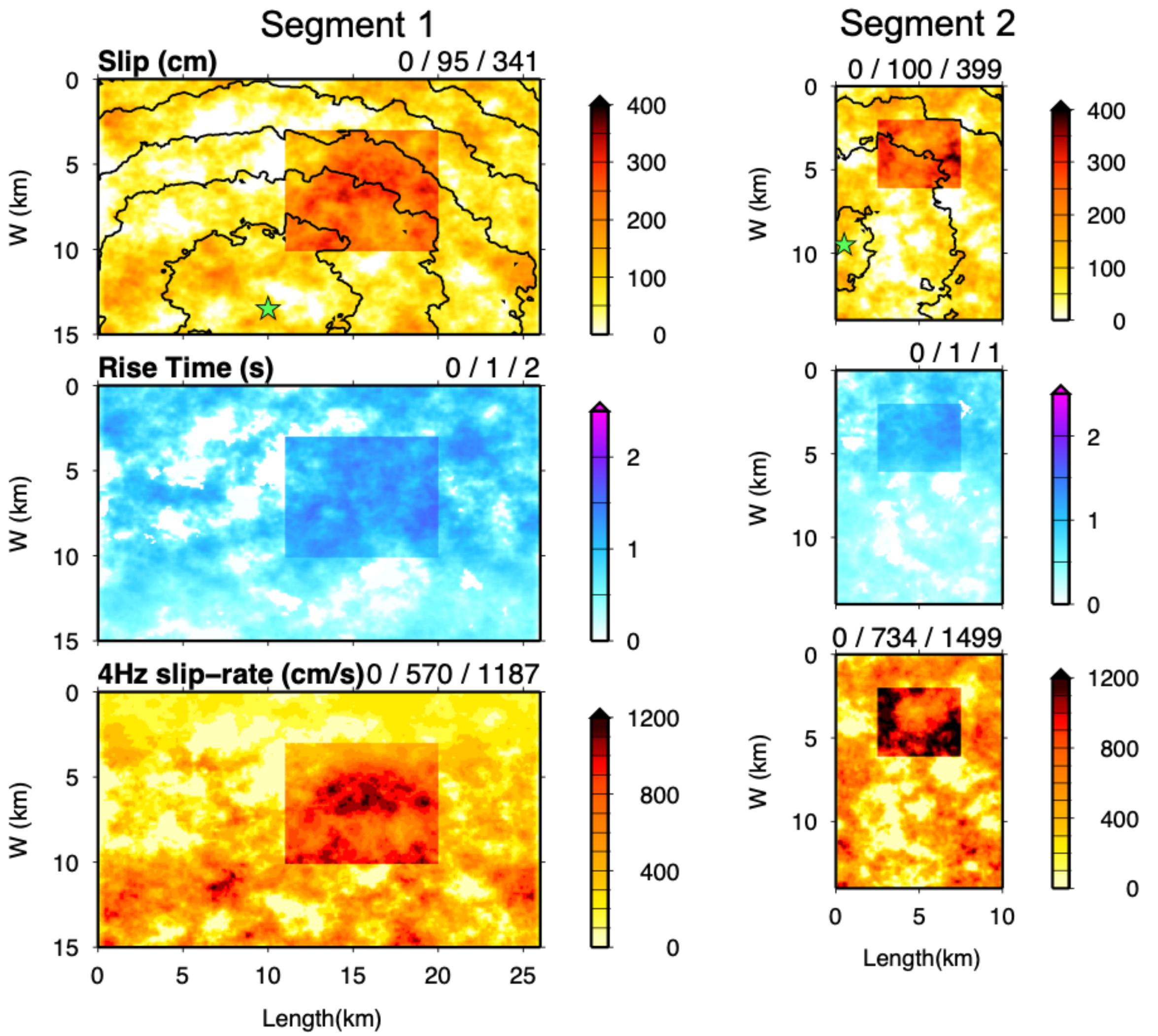

Figure 15. Kinematic rupture model for an M_w6.5 Norcia earthquake-type rupture scenario used in sensitivity analysis of simulated ground motion (Model 2). Left panel shows the main fault rupture while the right one shows the second fault segment. Top panels: Slip distribution and rupture time contours at 2 s intervals. Middle panels: rise time. Bottom panels: peak slip rate computed from the slip rate function low pass filtered at 4 Hz.

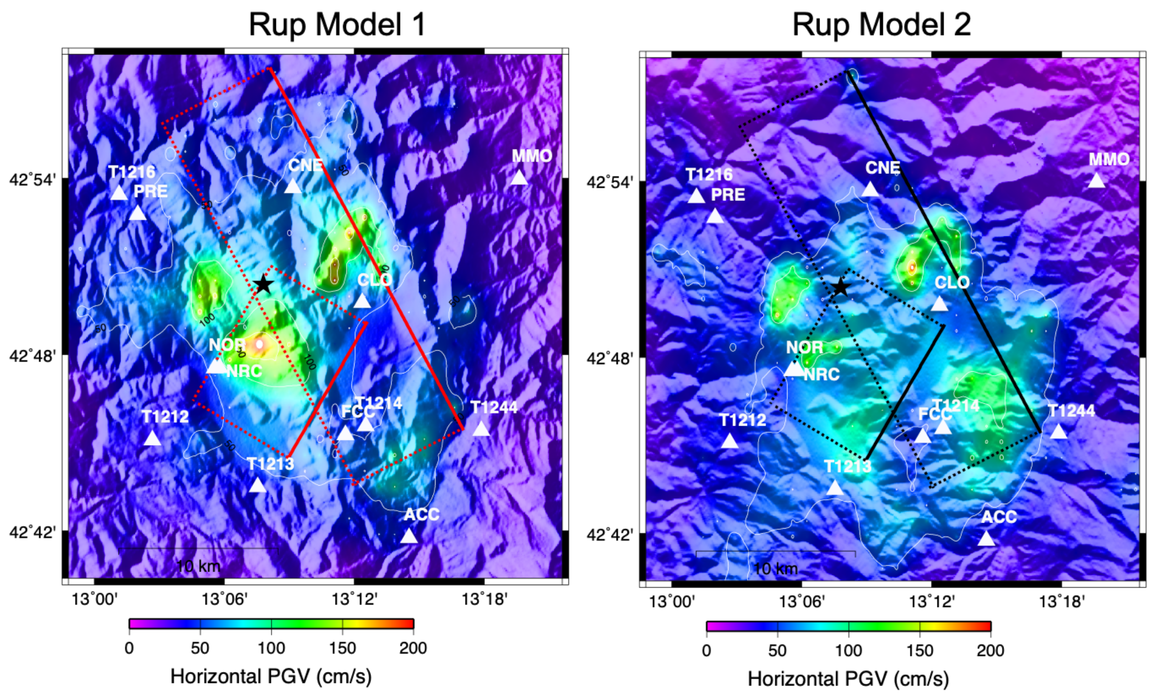

Figure 16. Maps of horizontal PGV computed with the M_w6.5 Norcia earthquake rupture model (left panel) and an M_w6.5 Norcia type earthquake rupture scenario Model (right panel). Dotted rectangles indicate the surface projections of the fault segments, solid lines indicate the surface projection of the top of the fault segments, and black star indicates the epicenter location. White triangles indicate the strong motion stations location. Note that the ground motion amplification pattern depends on the relative location of the large slip patches shown in **Figure 3** and **Figure 15**, for the rupture Model 1 and rupture Model 2, respectively.

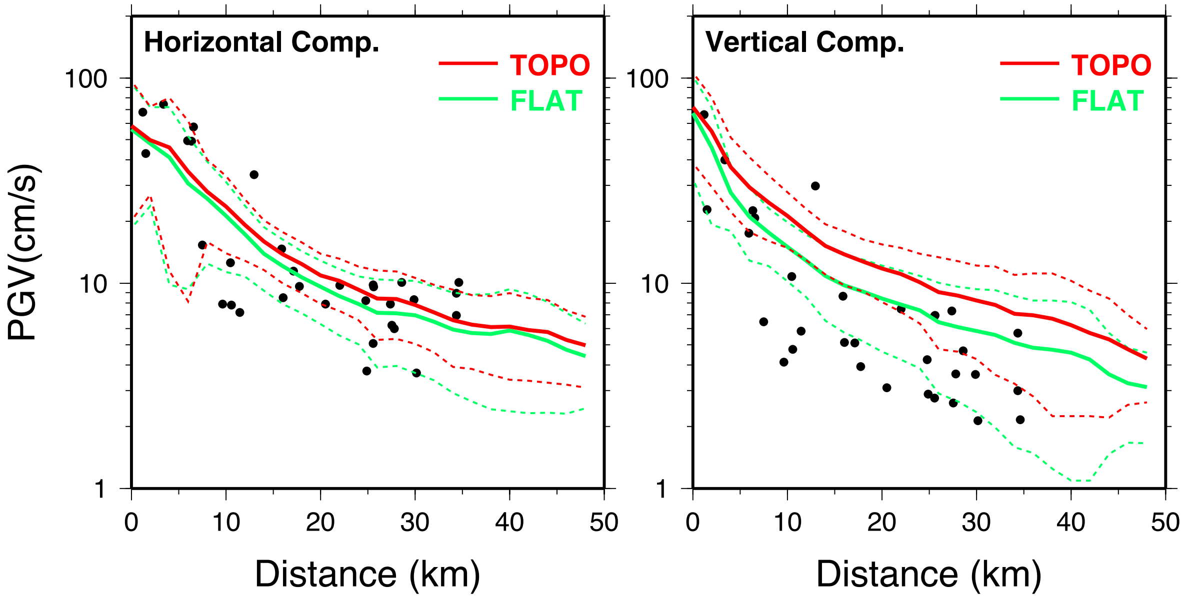

Figure 17. PGV computed on a grid of 8120 receivers with 1km spacing, covering the entire computational domain, plotted as a function of fault distance. Left panel corresponds to the horizontal PGV, and right panel corresponds to the vertical PGV. The red solid line indicates the median PGV computed with the 3D model with surface topography, and the green trace corresponds to the median PGV computed with the 3D model with flat free surface. The dotted lines correspond to median +/- one standard deviation. Black dots indicate the recorded PGV at 41 strong motion stations.

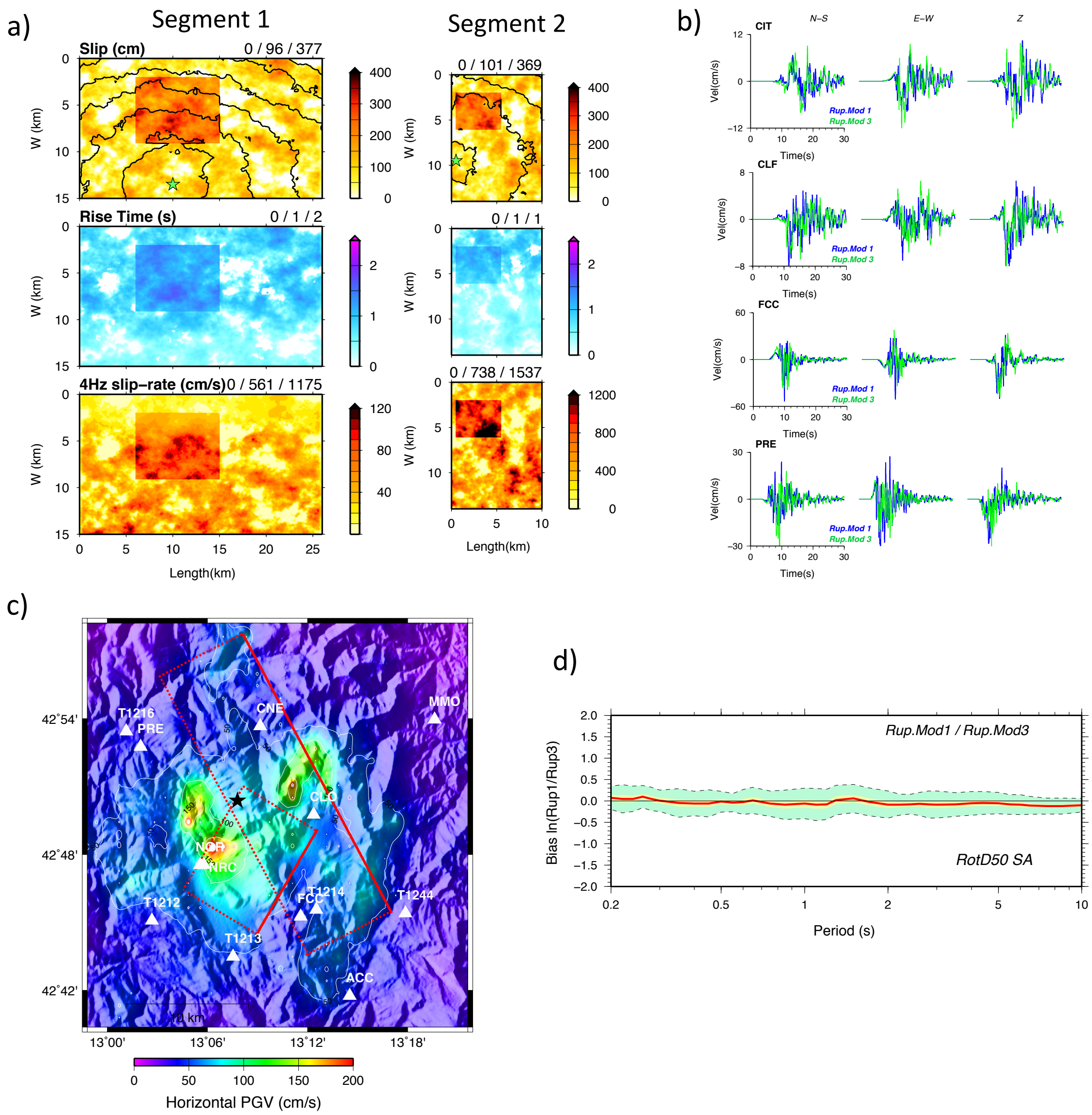

Figure 18. a) Strong motion simulation using rupture model Model 3 of the Norcia earthquake, b) Comparison of ground motion velocity at selected stations computed with rupture models Model 1 (blue traces), and Model 3 (green traces). The stations name is indicated on each panel, c) Map of simulated horizontal PGV, d) goodness-of-fit plot showing the bias (solid line) and standard deviation (dashed lines) of residuals between the simulated RotD50 spectral acceleration values computed with Model 1 and Model 3, in the period range 0.2 to 10 s, averaged over 41 stations.